Point-wise evaluation of the growth driving direction for arbitrarily shaped delamination fronts using cohesive elements

Carreras, Laura; Bak, B. L.V.; Turon, A.; Renart, J.; Lindgaard, E.

Published in:
European Journal of Mechanics, A/Solids

DOI (link to publication from Publisher):
10.1016/j.euromechsol.2018.05.006

Publication date:
2018

Document Version
Accepted author manuscript, peer reviewed version

Point-wise evaluation of the growth driving direction for arbitrarily shaped delamination fronts using cohesive elements

L. Carreras, B.L.V. Bak, A. Turon, J. Renart, E. Lindgaard

PII: S0997-7538(17)30778-7

DOI: 10.1016/j.euromechsol.2018.05.006

Reference: EJMSOL 3606

To appear in: *European Journal of Mechanics / A Solids*

Received Date: 17 October 2017

Revised Date: 4 March 2018

Accepted Date: 4 May 2018

Please cite this article as: Carreras, L., Bak, B.L.V., Turon, A., Renart, J., Lindgaard, E., Point-wise evaluation of the growth driving direction for arbitrarily shaped delamination fronts using cohesive elements, *European Journal of Mechanics / A Solids* (2018), doi: 10.1016/j.euromechsol.2018.05.006.

Point-wise evaluation of the growth driving direction for arbitrarily shaped delamination fronts using cohesive elements

L. Carreras[a,*], B.L.V. Bak[b], A. Turon[a], J. Renart[a], E. Lindgaard[b]

[a] *AMADE, Polytechnic School, University of Girona, Campus Montilivi s/n, E-17003 Girona, Spain*
[b] *Dept. of Materials and Production, Aalborg University, Fibigerstraede 16, DK-9220 Aalborg East, Denmark*

Abstract

The identification of the delamination propagation direction in three-dimensional structures with arbitrarily shaped fronts is needed in many applications. In the cohesive element framework, the propagation direction may be computed as the normal direction to a numerical damage isoline. The damage isoline tracking requires to exchange information between neighboring elements, thus post-processing global data, which is computationally expensive. This work presents a novel approach for the evaluation of the growth driving direction, only using local element information. The method can be directly implemented in a user-defined element subroutine and be evaluated at the execution time of the analysis. The presented formulation and its implementation in the commercial Finite Element code Abaqus is validated by comparison to the damage isoline shape rendering using global information.

Keywords:

Delamination growth, Cohesive zone model, Finite element analysis

1. Introduction

Long fiber-reinforced polymers are layered materials produced by stacking plies which contain continuous fibers in different orientations. Fibers supply stiffness and strength to the material in the laminate plane. Although laminated composite structures are designed so that the highest stresses are in the fiber directions, out-of-plane stresses may also occur at many types of geometric discontinuities

*Corresponding author. Tel.: +34 972 418 817
Email addresses: laura.carreras@udg.edu (L. Carreras), brianbak@mp.aau.dk (B.L.V. Bak), albert.turon@udg.edu (A. Turon), jordi.renart@udg.edu (J. Renart), elo@mp.aau.dk (E. Lindgaard)

ACCEPTED MANUSCRIPT

such as ply drops, skin-stiffener terminations, intersections, sandwich panels, free edges, holes, cut-outs, flanges, bonded and bolted joints or impacted zones. These load cases may damage the interface between plies, causing the failure mechanism called delamination. Delamination is considered the most detrimental failure mechanism in laminated composite structures because it occurs at relatively low load levels but still entails significant reduction of the structure's load carrying capacity. To address this problem without recoursing to impractical safe-life designs, damage-tolerant approaches are used. In that event, Finite Element (FE) analysis is an indispensable tool to predict delamination growth in complex laminated structures subjected to both static and fatigue loading.

The virtual crack closure technique (VCCT) is one of the most widely used FE techniques [1]. However, its application to realistic three-dimensional geometries with arbitrarily shaped crack front requires a continuous adaptive meshing technique in order to get a smooth front that fits with the instantaneous crack front curvature [2–4]. Alternative methods, that allow the use of stationary meshes, consist of tracing a smooth virtual front around the stepped front [5–7]. These techniques require the use of algorithms to determine the normal direction to the virtual delamination front using global information (or 18-noded elements as in [5]). This direction is used to compute the virtually closed area and to define a local coordinate system that enables to calculate the energy release rate components according to it.

An alternative to VCCT, is the cohesive zone model (CZM), firstly developed by Dugdale [8] and Barrenblatt [9]. In contrast with the VCCT approach, the application of the CZM is not limited to Linear Elastic Fracture Mechanics (LEFM). Indeed, it accounts for a large fracture process zone ahead of the crack tip where the material undergoes stiffness degradation until complete decohesion. This nonlinear material behavior is lumped into a surface, the cohesive zone, modeled by cohesive elements. Under static loading conditions, no crack tip tracking algorithm is required as long as the assumptions of identical fracture toughnesses for shear mode openings and independence of fracture toughness with propagation direction with respect to fiber orientation are made [10–17]. However, some of the existing methods for the simulation of fatigue-driven delamination using the CZM approach do require

ACCEPTED MANUSCRIPT

the identification of the propagation direction for its three-dimensional implementation [18–22], even making the same assumptions as in the static formulation. To the authors knowledge, the existing formulations to estimate the direction of crack propagation using CZM are nonlocal and, thus, require additional post-processing. In practice, these algorithms are computationally inefficient for the analysis of large structures.

Another and more recent approach presented by Van der Meer et al. [23] uses the level set method to describe the crack front location. Like the VCCT, it is a fracture mechanics approach. Furthermore, its variant for large process zone simulation [24] makes use of a stiffness degrading damage variable that allows a band of damaged material with predefined width. Conversely to most of the existing CZM formulations, the damage variable is not a function of the local properties but it is defined by the distance to the crack front, where the crack front is defined as the line that separates the damage process zone and the completely damaged interface.

In this work, a local algorithm to determine the growth driving direction in CZM is presented. It can be evaluated at any point within the cohesive zone at the same time the damage state is being computed. Therefore, it can be used to enhance the cohesive element formulation under static loading, preserving the local nature of the formulation. Moreover, it is an efficient alternative to the existing nonlocal propagation direction algorithms used in the methods for fatigue simulation.

The concept of growth driving direction applied to cohesive elements is presented in 2.1. Three different criteria for the growth driving direction identification are defined in Section 2.2. The formulation according to the first criterion is developed in Section 2.3. The formulation for the other two criteria is given in Appendix B. The three growth driving direction criteria are implemented for the particular case of the CZM presented in [15, 17], which is summarized in Appendix A. However, it is worth to mention that the same criteria could be applied to any other CZM formulation. Sections 3 and 4 present the results from the application of the formulation to three one-element case studies under different loading conditions and a real three-dimensional composite structure, respectively. The work closes by discussing the obtained results and with the conclusions.

ACCEPTED MANUSCRIPT

2. Determination of the growth driving direction

In the framework of LEFM, the propagation direction is assumed to be the normal direction to the crack front, where the crack front is the line separating the uncracked and cracked parts (see Figure 1.a). In contrast to LEFM, the CZM technique accounts for a band of damaged interface of variable length, called the fracture process zone, FPZ (light grey band in Figure 1.b). Therefore, the propagation direction, understood as the normal to the crack front line, can not be defined in the CZM framework. In this work, the concept of "growth driving direction"is introduced for CZM as the analogous to the propagation direction. It is assumed to be normal to a given damage isoline and can be calculated at any point within the FPZ. This definition follows naturally from the LEFM definition and provides the exact same result in the limiting case where the length of the fracture process zone goes to zero.

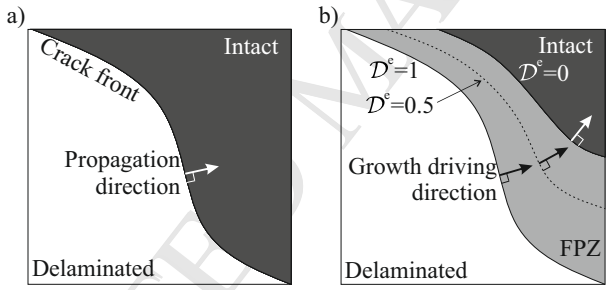

Figure 1: a) The propagation direction is assumed to be the normal direction to the crack front in the LEFM framework. b) The growth driving direction is assumed to be the normal direction to a damage isoline in the CZM framework. The energy-based damage variable, $\mathcal{D}^e$, is defined in Appendix A.

2.1. Growth driving direction using cohesive elements

Consider a laminated structure undergoing a delamination crack restricted to propagate in the interface between two adjacent plies. The degradation process of the material ahead of the crack tip is modeled in this work using the bilinear CZM formulation developed by Turon et al. in [15, 17]. As detailed in Appendix A, the process of the degradation of the interface properties is governed by an energy-based damage variable, $\mathcal{D}^e$, defined in Equation (A.16) as the ratio between the specific dissipated energy, ω_d, and the fracture toughness, $\mathcal{G}_c$. Thus, $\mathcal{D}^e$ is a scalar quantity that measures the

degree of crack development: when $\mathcal{D}^e$ equals 0, the degradation process is yet to start, while, when $\mathcal{D}^e$ equals 1, the crack is completely developed. The total specific work, ω_{tot}, corresponding to a given state of damage is the sum of the specific dissipated energy, ω_d, and the specific elastic energy, ω_e.

To ensure the proper energy dissipation under mixed-mode conditions, a one-dimensional cohesive law relates the equivalent mixed-mode traction, μ, to the equivalent mixed-mode displacement jump, λ. Such constitutive law is formed by an initial elastic region, before damage initiation, and a softening region. When the area under the one-dimensional traction-displacement jump curve is equal to the fracture toughness, $\mathcal{G}_c$, a new crack surface is formed. The Benzeggagh-Kenane criterion [25] is used to define the mixed-mode displacement jumps at which the onset of damage, λ_o, and propagation, λ_c, occur. A sketch of the equivalent one dimensional bilinear law is represented in Figure 2 for a given mode-mixity, B.

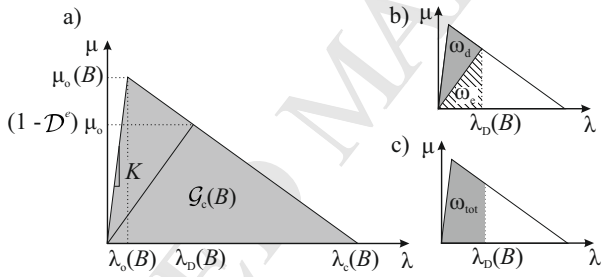

Figure 2: Equivalent one-dimensional cohesive law for a given mode-mixity, B. The shadowed area in a) represents the fracture toughness, $\mathcal{G}_c$, in b), the specific dissipated energy, ω_d, and the specific elastic energy, ω_e, and in c), the total specific work, ω_{tot}, for a given state of damage.

Complying with the cohesive element definition, the interfacial tractions and displacement jumps are evaluated at the interfacial deformed midsurface, $\overline{S}$, and determined by its local orientation. Thus, the normal and tangential traction components, acting on a unit deformed interfacial midsurface area, are conjugated to the normal and tangential displacement jumps across the material discontinuity. For the analysis of delamination propagation in three-dimensional structures, the interfacial midsurface is defined by the Cartesian coordinates $\overline{x}_i$, with $i = 1, 2, 3$. The local Cartesian coordinate system located on the deformed midsurface is defined by two tangential unit vectors, $\hat{\boldsymbol{e}}_1$ and $\hat{\boldsymbol{e}}_2$, and a normal unit vector, $\hat{\boldsymbol{e}}_3$. Assuming that the crack propagation is confined to the interface, the vector defining

the growth driving direction must belong to the plane spanned by the tangential vectors $\hat{\boldsymbol{e}}_1$ and $\hat{\boldsymbol{e}}_2$ at the point $\overline{p}_i$ where the direction is evaluated. Thus, the three-dimensional problem, can be solved in a two-dimensional space defined by the local Cartesian coordinates (e_1, e_2), where e_l, with $l = 1, 2$, are the coordinates spanned by the unit vectors $\hat{\boldsymbol{e}}_l$.

Then, for any given distribution of $\mathcal{D}^e\left(e_1, e_2\right)$, the growth driving direction at any point on the midsurface is assumed normal to the damage isolines, following the discussion related to Figure 1, i.e. is given by the negative of the gradient vector:

$$-\nabla \mathcal{D}^e\left(e_1, e_2\right) \tag{1}$$

2.2. Growth driving direction criteria

The growth driving direction at any point $\overline{p}_i$, contained in $\overline{S}$, is defined in this work as the one that provides the largest rate of decrease of $\mathcal{D}^e$. This is the direction of the negative gradient of $\mathcal{D}^e$, defined in the local Cartesian coordinate system (e_1, e_2) with origin at $\overline{p}_i$ (see Equation (1)). However, polar coordinates are most appropriate when looking for a direction from a pole (See Figure 3). Thus, the growth driving direction can be found by identifying the angle φ that minimizes the slope of $\mathcal{D}^e$ with respect to the radial coordinate, ρ:

$$\min_{\varphi} \frac{\partial \mathcal{D}^e}{\partial \rho} \tag{2}$$

Considering the energy-based damage, $\mathcal{D}^e$, dependent on both the mode mixity, B, and the mixed-mode displacement jump, λ, and by application of the chain rule, the angle φ that minimizes Equation (2) can be found by solving:

$$\frac{\partial}{\partial \varphi} \frac{\partial \mathcal{D}^e\left(B, \lambda\right)}{\partial \rho} = \frac{\partial}{\partial \varphi} \left(\frac{\partial \mathcal{D}^e}{\partial B} \frac{\partial B}{\partial \rho} + \frac{\partial \mathcal{D}^e}{\partial \lambda} \frac{\partial \lambda}{\partial \rho} \right) = 0 \tag{3}$$

and by checking its convexity:

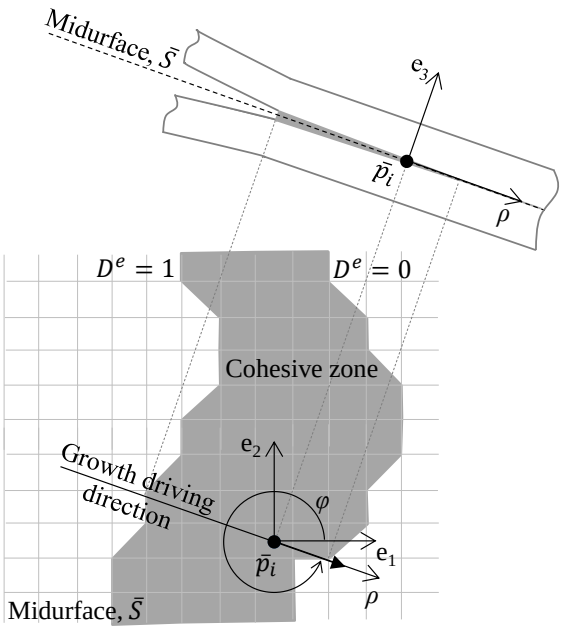

Figure 3: The growth driving direction evaluated at point $\bar{p}_i$ is embedded in the tangential plane spanned by the local Cartesian coordinates e_1 and e_2.

$$\frac{\partial^2}{\partial \varphi^2}\frac{\partial \mathcal{D}^e\left(B,\lambda\right)}{\partial \rho} = \frac{\partial^2}{\partial \varphi^2}\left(\frac{\partial \mathcal{D}^e}{\partial B}\frac{\partial B}{\partial \rho} + \frac{\partial \mathcal{D}^e}{\partial \lambda}\frac{\partial \lambda}{\partial \rho}\right) > 0 \tag{4}$$

However, equations (3) and (4) are equal to zero in the elastic regime ($\lambda \in [0, \lambda_o]$), since the energy based damage variable, $\mathcal{D}^e$, is also equal to zero (see Equation (A.16). In order to compute the growth driving direction before the initiation of the degradation process, another criterion, based on the ratio between the total specific work, ω_{tot} and the fracture toughness, $\mathcal{G}_c$, can be formulated such that the growth driving direction can be found by solving:

$$\min_{\varphi} \frac{\partial\left(\frac{\omega_{tot}}{\mathcal{G}_c}\left(B,\lambda\right)\right)}{\partial \rho} \tag{5}$$

Note that, similarly to the energy-based damage, $\mathcal{D}^e$, the ratio between the total specific work and the fracture toughness, $\frac{\omega_{tot}}{\mathcal{G}_c}$, is dependent on both the mode mixity, B, and the mixed-mode displacement jump, λ.

Finally, for the sake of simplicity, a third criterion, which is also active before damage initiation,

can be formulated only taking into account the mixed-mode displacement jump field, λ:

$$\min_{\varphi} \frac{\partial \lambda}{\partial \rho} \tag{6}$$

The general expressions to solve for each of the criteria are listed in Table B.5.

In summary, three different criteria are presented depending on the quantity being analyzed: the energy-based damage, $\mathcal{D}^e$, (Criterion 1), the total specific work over the fracture toughness, $\frac{\omega_{tot}}{\mathcal{G}_c}$ (Criterion 2), and the mixed-mode displacement jump, λ, (Criterion 3). The evolution of these quantities along the growth driving direction are sketched in Figure 4 for an interface opened under pure mode I conditions. The three criteria are listed in Table 1 and presented in the following.

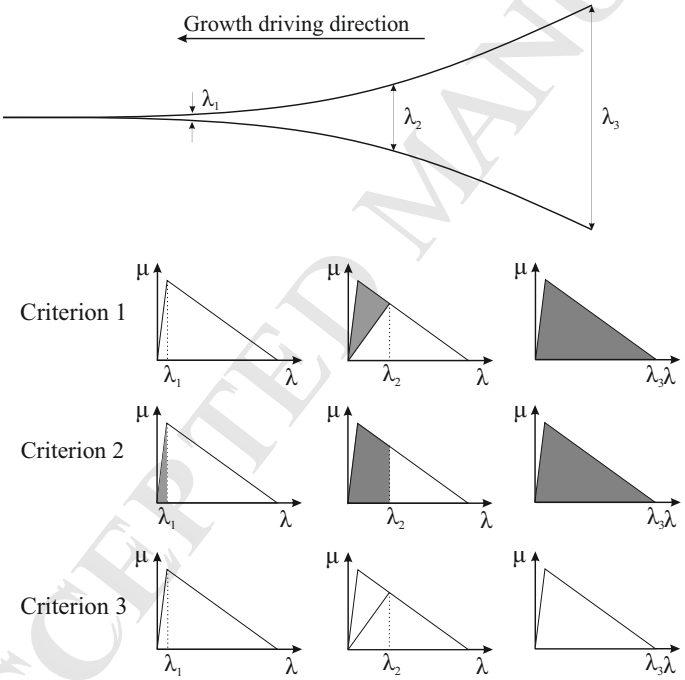

Figure 4: Quantities being minimized in each criterion for a pure mode I opened interface.

Criterion 1. The growth driving direction is defined by the negative gradient of the energy-based damage variable, $\mathcal{D}^e$. This is equivalent to computing the negative gradient of the ratio between the specific dissipated energy, ω_d (see Figure 2.b), and the fracture toughness, $\mathcal{G}_c$. Since Criterion 1 is based on the energy-based damage distribution, $\mathcal{D}^e$, it is only active once the degradation process is

ACCEPTED MANUSCRIPT

Criterion ID	Function to solve	Nomenclature	Approach	Limitations
1	$-\nabla\mathcal{D}^e$	$\mathcal{D}^e$: Energy-based damage	Energy-based	Not active in elastic regime
2	$-\nabla\frac{\omega_{tot}}{\mathcal{G}_c}$	ω_{tot}:total specific work $\mathcal{G}_c$: fracture toughness	Energy-based	May depend on the specific elastic energy in CZM
3	$-\nabla\lambda$	λ: mixed-mode opening displacement	Geometrical	Independent of interface properties

Table 1: Summary of the criteria to determine the growth driving direction.

already initiated. Moreover, Criterion 1 is an energy-based approach that depends on the kinematics and the constitutive law of the cohesive element. Since the cohesive law is usually mode-dependent, an uneven distribution of mode-mixity, B, can affect the gradient vector.

Criterion 2. The growth driving direction is defined by the negative gradient of the ratio between the total specific work, ω_{tot} (see Figure 2.c), and the fracture toughness, $\mathcal{G}_c$. Thus, both the specific dissipated energy, ω_d and the specific elastic energy, ω_e, are included in the computation of Criterion 2. Since, as soon as two initially coinciding points separate from each other some elastic energy is stored, Criterion 2 is active before any energy dissipation due to fracture takes place. Moreover, this approach depends on both the kinematics and the constitutive law of the cohesive element and, therefore, can be affected by the variation in mode-mixity, B, with the direction.

It is worth to mention that, with the constitutive model used in this work, presented in Appendix A.2, criteria 1 and 2 lead to the same growth driving direction results. However, since both the conservative and non-conservative work are computed in Criterion 2, in contrast to Criterion 1, in which only the non-conservative work is quantified, both criteria might provide different results when using other CZ formulations that allow the definition of mode-dependent penalty stiffness, K [26].

Criterion 3. The growth driving direction is defined by the negative gradient of the mixed-mode displacement jump, λ. This is a pure geometrical approach, since the only governing parameter is the mixed-mode displacement jump. Thus, the solution only depends on the kinematics of the cohesive element. Indeed, changes in the cohesive law due to variation in mode-mixity, B, with direction are

ACCEPTED MANUSCRIPT

not affecting Criterion 3.

2.3. Formulation of Criterion 1 for the identification of the growth driving direction

A complete description of the derivation of Criterion 1 is presented in this section. Moreover, the formulation for the evaluation of the growth driving direction using criteria 2 and 3 is given in Appendix B.

It can be seen, from equations (3) and (4), that, in order to find the growth driving direction using Criterion 1, the radial slope of the energy-based damage, $\frac{\partial \mathcal{D}^e}{\partial \rho}$, must be minimized as a function of the angle φ. Each of the terms in equations (3) and (4) are derived in the following.

The derivative of the energy-based damage with respect to the mode mixity, $\frac{\partial \mathcal{D}^e}{\partial B}$, and the derivative of the energy-based damage with respect to the mixed-mode displacement jump, $\frac{\partial \mathcal{D}^e}{\partial \lambda}$, are scalar factors that depend on the parameters defining the CZM. The expression for $\frac{\partial \mathcal{D}^e}{\partial B}$ obtained after the particular application to the CZM from [15, 17] is:

$$\frac{\partial \mathcal{D}^e}{\partial B} = \frac{\eta \left(\mathcal{G}_{IIc} - \mathcal{G}_{Ic}\right) B^{(\eta-1)} \lambda}{K \lambda_c \lambda_o \left(\lambda_o - \lambda_c\right)} = F_B \tag{7}$$

and the expression for $\frac{\partial \mathcal{D}^e}{\partial \lambda}$ reads:

$$\frac{\partial \mathcal{D}^e}{\partial \lambda} = \frac{1}{\lambda_c - \lambda_o} = F_\lambda \tag{8}$$

Furthermore, the radial slope of the mixed-mode displacement jump, $\frac{\partial \lambda}{\partial \rho}$, in equations (3) and (4) is addressed in the following. Taking into account the dependency of the mixed-mode displacement jump, λ (Equation (A.7)), on the normal and tangential displacement jumps, arranged in vector δ_i, and by application of the chain rule, the following expression is obtained:

$$\frac{\partial \lambda}{\partial \rho} = \frac{\partial \lambda}{\partial \delta_j} \frac{\partial \delta_j}{\partial \rho} \tag{9}$$

The first term in the right hand side of Equation (9) reads:

ACCEPTED MANUSCRIPT

$$\frac{\partial \lambda}{\partial \delta_j} = \left\{ \frac{\delta_1}{\lambda},\ \frac{\delta_2}{\lambda},\ \frac{\langle \delta_3 \rangle}{\lambda} \right\}^T = A_j \tag{10}$$

and the second term in the right hand side of Equation (9) is the derivative of the displacement jumps, δ_j, with respect to the radial coordinate, ρ, which is obtained as follows:

$$\frac{\partial \delta_j}{\partial \rho} = \frac{\partial \Theta_{ji}}{\partial \rho} M_{im} Q_m + \Theta_{ji} \frac{\partial M_{im}}{\partial \rho} Q_m \tag{11}$$

where Θ_{ji} is the rotation matrix that relates the global to the local Cartesian coordinate system and M_{im} is the transformation matrix that relates the global displacement jump with the nodal global displacement, Q_m (see Appendix A).

The derivative of the rotation matrix, Θ_{ji}, with respect to the radial coordinate, ρ, can be approximated to zero, by assuming that the curvature of the interface within the element domain is small. Moreover, its derivation leads to a complex expression that would increase the difficulty of the formulation and its further implementation into FE without a substantial improvement in the accuracy of the solution. For the sake of simplicity, in the following it is assumed that $\frac{\partial \Theta_{ji}}{\partial \rho} = 0$. Therefore, only the second summand in the right hand side of Equation (11) is addressed.

The derivative of the transformation matrix, M_{im}, with respect to the local polar coordinate, ρ, is obtained by successive application of the chain rule:

$$\frac{\partial M_{im}}{\partial \rho} = \frac{\partial M_{im}}{\partial \eta_\alpha} \frac{\partial \eta_\alpha}{\partial e_l} \frac{\partial e_l}{\partial \rho} \tag{12}$$

The first partial derivative in the right hand side of Equation (12) is the variation of the transformation matrix, M_{im}, with the isoparametric coordinates of the cohesive element formulation, η_α (see Appendix A):

$$\frac{\partial M_{im}}{\partial \eta_\alpha} = \left[-\frac{\partial N_{ik}}{\partial \eta_\alpha},\ \frac{\partial N_{ik}}{\partial \eta_\alpha} \right] = E_{im\alpha} \tag{13}$$

ACCEPTED MANUSCRIPT

where N_{ik} is the shape function matrix and the subscript k runs from 1 to the number of degrees of freedom of each of top and bottom surface of the cohesive element. In case of an eight-noded element, $k = 1...12$.

The derivative $\frac{\partial \eta_\alpha}{\partial e_l}$ is the inverse matrix of the two vectors tangential to the deformed midsurface, described in Equation (A.2) and expressed in local tangential coordinates, these being:

$$\frac{\partial e_l}{\partial \eta_\alpha} = \Theta_{li} \frac{1}{2} \frac{\partial N_{ik}}{\partial \eta_\alpha} \left(C_k^+ + C_k^- + Q_k^+ + Q_k^- \right) = \Theta_{li} J_{i\alpha} \tag{14}$$

where $J_{i\alpha}$ is the Jacobian matrix defined in Equation (A.26). Thus, let matrix $G_{\alpha l}$ be defined as:

$$G_{\alpha l} = \left(\Theta_{li} J_{i\alpha} \right)^{-1} = \begin{bmatrix} \frac{\partial \eta_1}{\partial e_1} & \frac{\partial \eta_2}{\partial e_1} \\ \frac{\partial \eta_1}{\partial e_2} & \frac{\partial \eta_2}{\partial e_2} \end{bmatrix} \tag{15}$$

Using the following transformation relation:

$$\begin{bmatrix} e_1 \\ e_2 \end{bmatrix} = \begin{bmatrix} \rho \ \cos(\varphi) \\ \rho \ \sin(\varphi) \end{bmatrix} \tag{16}$$

the derivative of the local Cartesian coordinates, e_l, with respect to the radial coordinate, ρ, reads:

$$\frac{\partial e_l}{\partial \rho} = \begin{bmatrix} \cos(\varphi) \\ \sin(\varphi) \end{bmatrix} \tag{17}$$

Then, the slope of the mixed-mode displacement jump, λ, with respect to the radial coordinate, ρ, is obtained using equations (10)-(17) in Equation (9):

$$\frac{\partial \lambda}{\partial \rho} = A_j \Theta_{ji} E_{im\alpha} \left(G_{\alpha 1} \left(\cos \varphi \right) + G_{\alpha 2} \left(\sin \varphi \right) \right) Q_m \tag{18}$$

The same procedure can be applied to find the radial slope of the mode mixity, $\frac{\partial B}{\partial \rho}$, in equations (3) and (4). Taking into account the dependency of the mode mixity, B, defined in Equation (A.10),

on the displacement jumps, δ_j, the radial slope $\frac{\partial B}{\partial \rho}$ is obtained by applying the chain rule as:

$$\frac{\partial B}{\partial \rho} = \frac{\partial B}{\partial \delta_j} \frac{\partial \delta_j}{\partial \rho} \tag{19}$$

where the derivative of the mode mixity, B, with respect to the displacement jumps, δ_j, reads:

$$\frac{\partial B}{\partial \delta_j} = \left\{ \frac{2\delta_1 \langle \delta_3 \rangle^2}{\lambda^4},\ \frac{2\delta_2 \langle \delta_3 \rangle^2}{\lambda^4},\ -\frac{2\delta_s^2 \langle \delta_3 \rangle}{\lambda^4} \right\}^T = O_j \tag{20}$$

and $\frac{\partial \delta_j}{\partial \rho}$ is developed through equations (11)-(17). Hence, the radial slope $\frac{\partial B}{\partial \rho}$ is given by:

$$\frac{\partial B}{\partial \rho} = O_j \Theta_{ji} E_{im\alpha} \left(G_{\alpha 1} \left(\cos \varphi \right) + G_{\alpha 2} \left(\sin \varphi \right) \right) Q_m \tag{21}$$

Finally, let matrix V_α be:

$$V_\alpha = F_B O_j \Theta_{ji} E_{im\alpha} Q_m \tag{22}$$

and matrix W_α be:

$$W_\alpha = F_\lambda A_j \Theta_{ji} E_{im\alpha} Q_m \tag{23}$$

then, the growth driving direction according to Criterion 1 is found using equations (18) and (21)-(23) in Equation (3), solving for the angular coordinate, φ:

$$\varphi = \operatorname{atan} \left(-\frac{\left(V_1 + W_1 \right) G_{11} + \left(V_2 + W_2 \right) G_{21}}{\left(V_1 + W_1 \right) G_{12} + \left(V_2 + W_2 \right) G_{22}} \right) \tag{24}$$

and fulfilling the condition for convexity (Equation (4)):

$$\left(V_\alpha + W_\alpha \right) \left(G_{\alpha 1} \left(-\cos \varphi \right) + G_{\alpha 2} \left(-\sin \varphi \right) \right) > 0 \tag{25}$$

Once φ is identified, the transformation of the global Cartesian coordinates, X_i, into the local

ACCEPTED MANUSCRIPT

Cartesian coordinates that are located on the midsurface and oriented according to the growth driving direction is done by means of the following rotation matrix:

$$R_{ri} = T_{rj}\Theta_{ji} \tag{26}$$

where T_{rj} is:

$$T_{rj} = \begin{bmatrix} \cos\varphi & -\sin\varphi & 0 \\ \sin\varphi & \cos\varphi & 0 \\ 0 & 0 & 1 \end{bmatrix} \tag{27}$$

As shown, all the information necessary to evaluate Criterion 1 (and also criteria 2 and 3, as demonstrated in Appendix B) are the global nodal coordinates, C_m and displacements Q_m. Using the cohesive element formulation in [15, 17], this information is available at the element level and, thus, the presented growth driving direction algorithms can be implemented into a user-defined element subroutine and evaluated at any point in the cohesive zone without any additional post-processing or non-local information.

3. One-element validation examples

The following one-element studies serve to validate the formulation of the growth driving direction criteria presented in Section 2. The proposed method has been implemented in a MATLAB program. The eight-noded cohesive element used is illustrated in Figure 5. The kinematics and constitutive law associated to the element are detailed in Appendix A. Newton-Cotes integration scheme is used, with 2x2 integration points located at the midsurface vertexes. The undeformed element is 0.1 mm wide, 0.1 mm long and has zero thickness. The cohesive properties are listed in Table 2. Three different loading cases (A, B and C) have been analyzed. The applied nodal displacement is listed in Table 3 for each case. The growth driving direction is calculated at a point $\overline{\boldsymbol{p}}\,(\eta_1, \eta_2)$ located on the midsurface, with natural coordinates $(-0.5, -0.5)$. The results of the angle φ obtained in each case are listed in

ACCEPTED MANUSCRIPT

Interface properties		
$\mathcal{G}_{Ic}$	0.3	N/mm
$\mathcal{G}_{IIc}$	0.7	N/mm
τ_{Ic}	50	MPa
τ_{IIc}	76.4	MPa
η	2	-
K	1E5	N/mm^3

Table 2: Cohesive law properties used in the one-element case studies.

Case ID	Loading conditions	Nodal displacements (mm)	φ at point $\overline{\boldsymbol{p}}$ (deg) Criterion 1	Criterion 2	Criterion 3
A	Pure mode I B constant	$u_3^5 = 0.005$ $u_3^6 = 0.005$ $u_3^7 = 0.01$ $u_3^8 = 0.01$	270.0	270.0	270.0
B	Mixed mode I-shear B constant	$u_1^5 = u_2^5 = u_3^5 = 0.001$ $u_1^6 = u_2^6 = u_3^6 = 0.002$ $u_1^7 = u_2^7 = u_3^7 = 0.003$ $u_1^8 = u_2^8 = u_3^8 = 0.002$	225.3	225.3	225.3
C	Mixed mode I-shear same λ at nodes	$u_1^5 = \sqrt{2 \cdot 0.008}$ $u_1^6 = u_3^6 = 0.008$ $u_3^7 = \sqrt{2 \cdot 0.008}$ $u_1^8 = u_3^8 = 0.008$	225.0	225.0	45.0

Table 3: Loading conditions and growth driving direction results at point $\overline{\boldsymbol{p}}$ from the one-element case studies

Table 3 for the three criteria.

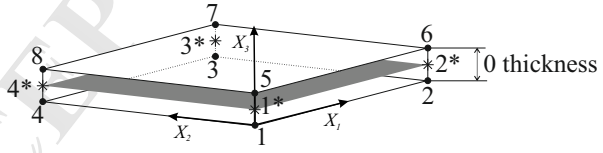

Figure 5: Sketch of the undeformed cohesive element. The nodes are represented as black dots and numbered from 1 to 8 and the integration points are represented as asterisks and numbered from 1* to 4*.

Case A is a pure mode I-opened element. The distribution of the mixed-mode displacement jump, λ, along the element midsurface is projected on the deformed element midsurface in Figure 6, where the point $\overline{\boldsymbol{p}}$ is highlighted in white. Integation points 1 and 2 have the lowest λ value, while points 3 and 4 are the most opened. As illustrated, the growth driving direction according to Criterion 3

is determined by the greatest rate of decrease of λ. The other quantities being analyzed in criteria 1 and 2, $\mathcal{D}^e$ and $\frac{\omega_{tot}}{\mathcal{G}_c}$ respectively, are represented in Figure 7, as well as the mode-mixity, B. Like the B-distribution along the element midsurface is constant, the growth driving direction is only defined by the direction that minimizes the slope of the mixed-mode displacement jump. Therefore, in Case A only, the kinematics of the element governs the growth driving direction, independently of which criteria is used.

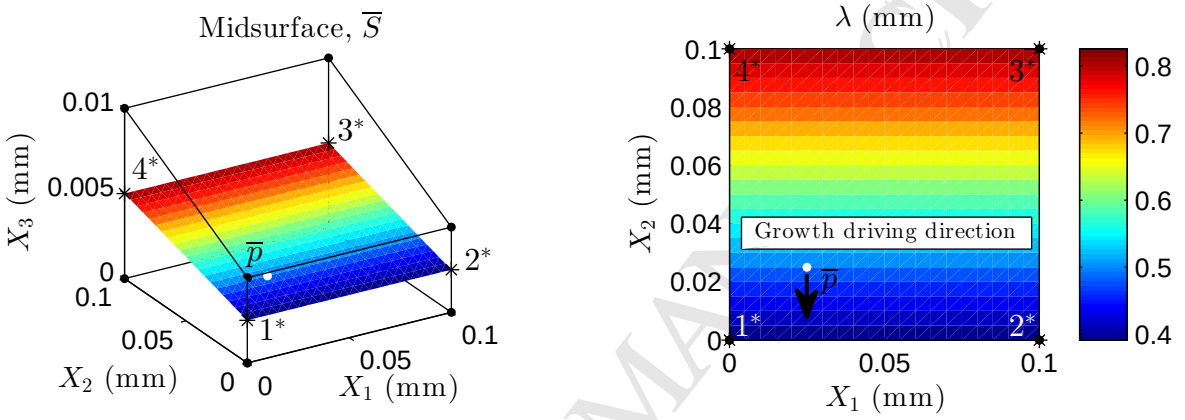

Figure 6: Mixed-mode displacement jump distribution at the element midsurface for Case A loading conditions. The growth driving direction is analyzed at point $\overline{\boldsymbol{p}}$, indicated with a white circle, and the result is listed in Table 3.

On the other hand, in Case B, the element is opened under constant mixed mode I-shear opening conditions (See Figure 8). In this case, λ linearly increases along the midsurface diagonal direction, from integration point 1 to integration point 3. However, B is constant and, thus, also the constitutive law associated to it. Again, in Case B, the growth driving direction is only defined by the direction that minimizes the slope of the mixed-mode displacement jump, λ. Therefore, it is governed by the kinematics of the cohesive element and there is agreement between the three criteria.

Finally, in Case C, all the integration points have the same λ-value, although the mode-mixity, B, changes from 0 to 1 along the midsurface diagonal direction (See Figure 9). At integration point 1, only shear sliding displacement is applied, while at the opposite corner, at integration point 3, there is only mode I opening. At the integration points 2 and 4, there is 50% mixed-mode opening. On the other

hand, λ is lower at the center part of the element midsurface than at the corners and its distribution is determined by the interpolation functions. Criterion 3 is only affected by the λ-interpolation and results in the direction that points to the center of the element. Furthermore, due to the uneven B-distribution, the constitutive law is not constant. With the cohesive properties used in these studies, the direction of steepest negative slopes of $\mathcal{D}^e$ and $\frac{\omega_{tot}}{\mathcal{G}_c}$ coincides with the direction that maximizes the rate of increase of B. Note that, when evaluated at point $\overline{\boldsymbol{p}}$, this is the direction of largest slope of λ. Therefore, Criterion 3 and criteria 1 and 2 point to opposite directions.

In addition, the slopes $\frac{\Delta\mathcal{D}^e}{\Delta\rho}$, $\frac{\Delta(\omega_{tot}/\mathcal{G}_c)}{\Delta\rho}$ and $\frac{\Delta\lambda}{\Delta\rho}$ have been numerically evaluated using a central difference at every 1 degree at point $\overline{\boldsymbol{p}}$ under Case C loading conditions using a perturbation size for the radius of 0.001 mm. Thus, the slope of any quantity f has been calculated as:

$$\frac{\Delta f}{\Delta\rho} = \frac{f(0.001,\varphi) - f(-0.001,\varphi)}{2 \cdot 0.001} \tag{28}$$

The resulting slopes are represented in Figure 10. The disagreement between Criterion 3 and criteria 1 and 2 can be observed. For Criterion 3, the angle φ that minimizes $\frac{\Delta\lambda}{\Delta\rho}$ is 45 degrees, while for criteria 1 and 2, the angle that minimizes $\frac{\Delta\mathcal{D}^e}{\Delta\rho}$ and $\frac{\Delta(\omega_{tot}/\mathcal{G}_c)}{\Delta\rho}$, respectively, amounts 225 degrees. Note that these results are in agreement with the results obtained by implementing the formulation developed in Section 2.

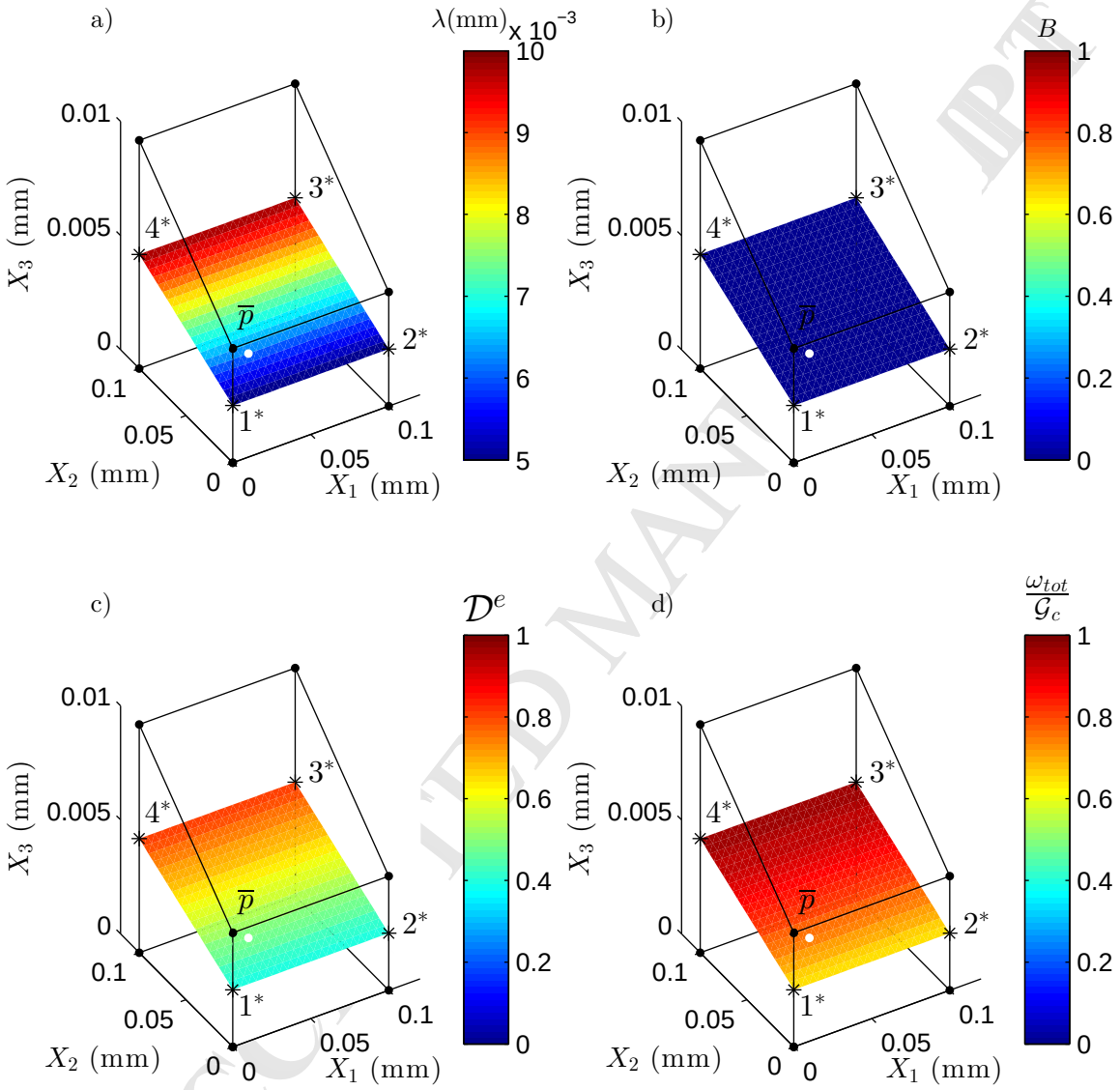

Figure 7: a) Mixed-mode displacement jump, λ, b) mode-mixity, B, c) energy-based damage, $\mathcal{D}^e$, and d) total specific work over the fracture toughness, $\frac{\omega_{tot}}{\mathcal{G}_c}$, distributions at the element midsurface for Case A loading conditions. The point $\overline{\boldsymbol{p}}$, where the growth driving direction is analyzed, is indicated with a white circle.

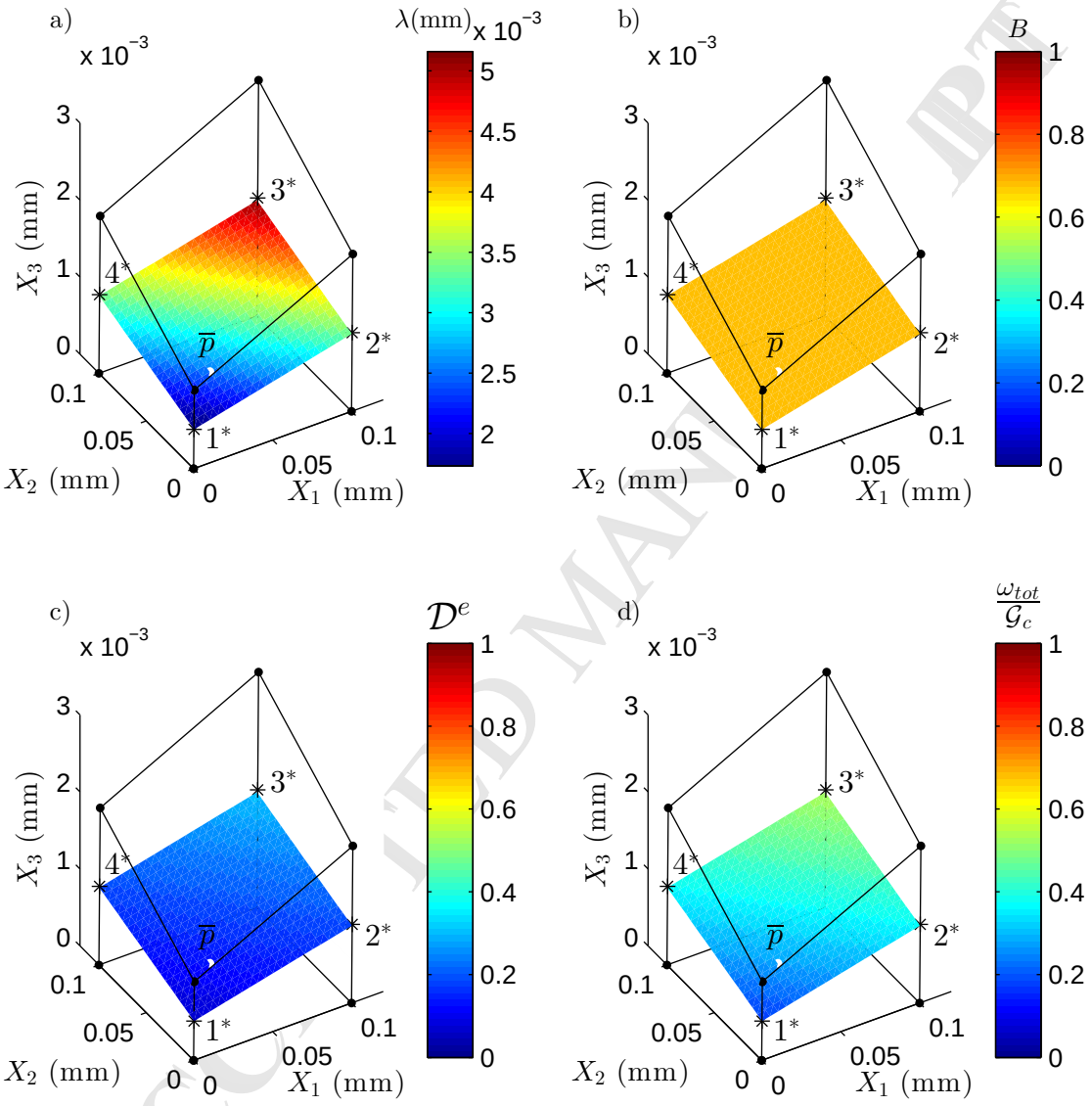

Figure 8: a) Mixed-mode displacement jump, λ, b) mode-mixity, B, c) energy-based damage, $\mathcal{D}^e$, and d) total specific work over the fracture toughness, $\frac{\omega_{tot}}{\mathcal{G}_c}$, distributions at the element midsurface for Case B loading conditions. The point $\overline{\boldsymbol{p}}$, where the growth driving direction is analyzed, is indicated with a white circle.

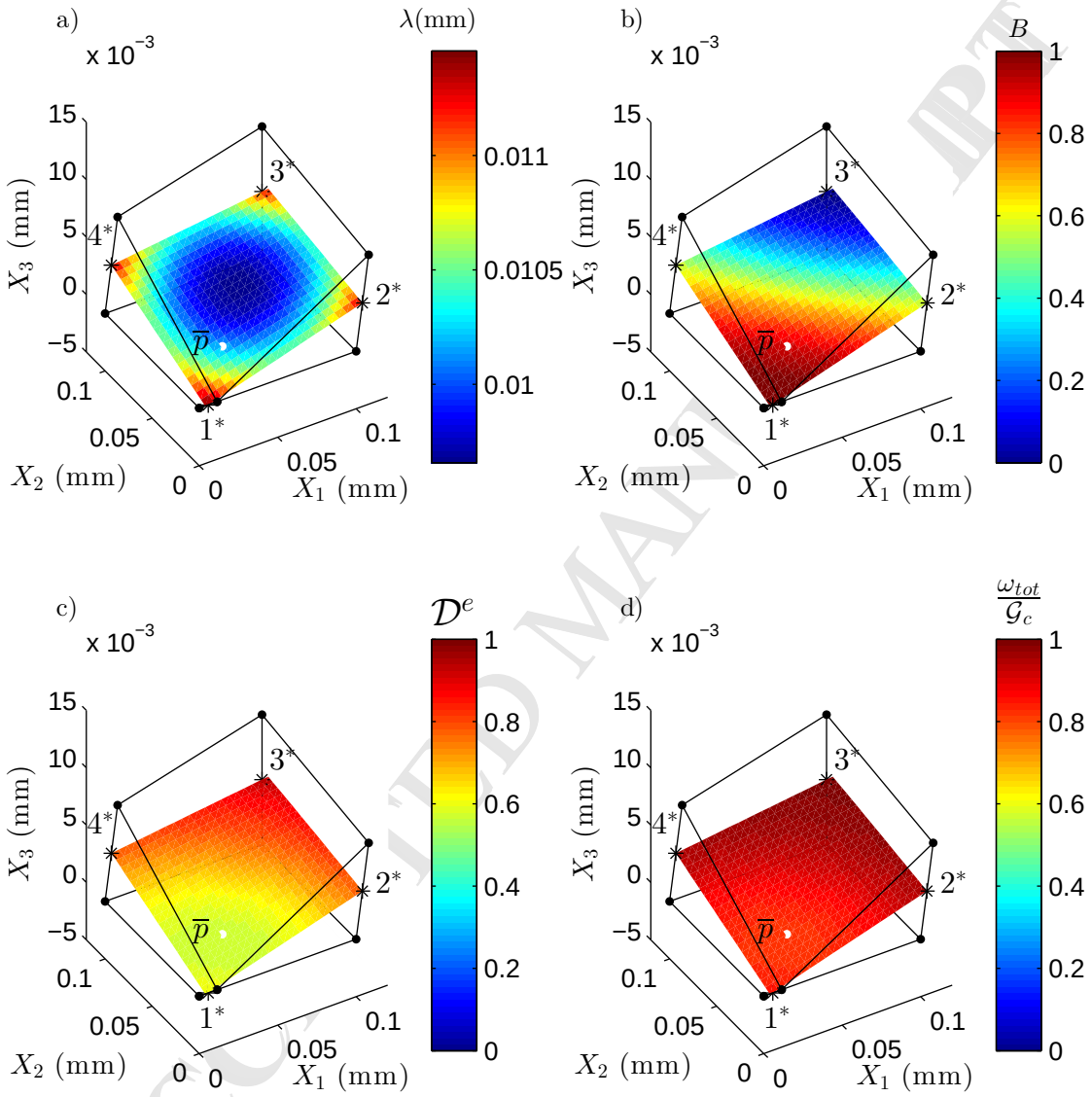

Figure 9: a) Mixed-mode displacement jump, λ, b) mode-mixity, B, c) energy-based damage, $\mathcal{D}^e$, and d) total specific work over the fracture toughness, $\frac{\omega_{tot}}{\mathcal{G}_c}$, distributions at the element midsurface for Case C loading conditions. The point $\overline{\boldsymbol{p}}$, where the growth driving direction is analyzed, is indicated with a white circle.

ACCEPTED MANUSCRIPT

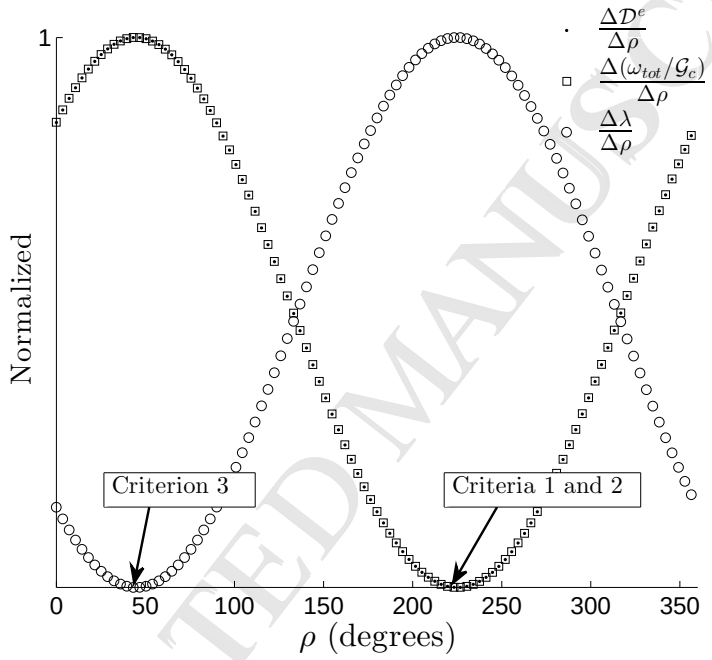

Figure 10: Slopes in the radial direction, ρ, of the energy-based damage, $\mathcal{D}^e$, the total specific work over the fracture toughness, $\frac{\omega_{tot}}{\mathcal{G}_c}$, and the mixed-mode displacement jump, λ, as a function of the angle φ evaluated at point $\overline{\boldsymbol{p}}$ for Case C loading conditions. The slopes have been calculated using a central difference with a perturbation for the radius of 0.001 mm. The values $\frac{\Delta \mathcal{D}^e}{\Delta \rho}$, $\frac{\Delta(\omega_{tot}/\mathcal{G}_c)}{\Delta \rho}$ and $\frac{\Delta \lambda}{\Delta \rho}$ have been normalized by their maximum value.

4. Three-Dimensional application

To exemplify the applicability of the presented formulation, a three-dimensional model with a non-straight crack front is used. The test configuration is a End-Loaded Split (ELS) test on a symmetric run-out specimen with a midplane initial defect. A Teflon insert acts as an initial straight delamination (see Figure 11). Moreover, the middle width of the specimen is stiffened by bonding CFRP reinforcements on the upper and lower faces. During propagation the crack front shape changes when it approaches the reinforced region. The formulation presented in Section 2 can be used to evaluate the growth driving criteria at any given loading state during the quasi-static simulation. To this end, the method in [15, 17] has been enhanced with the growth driving direction calculation and implemented in Abaqus [27] as a UEL subroutine. The user-defined cohesive elements that model the middle interface are 0.2 mm x 0.5 mm. The laminate and interface properties used in the simulation are listed in Table 4.

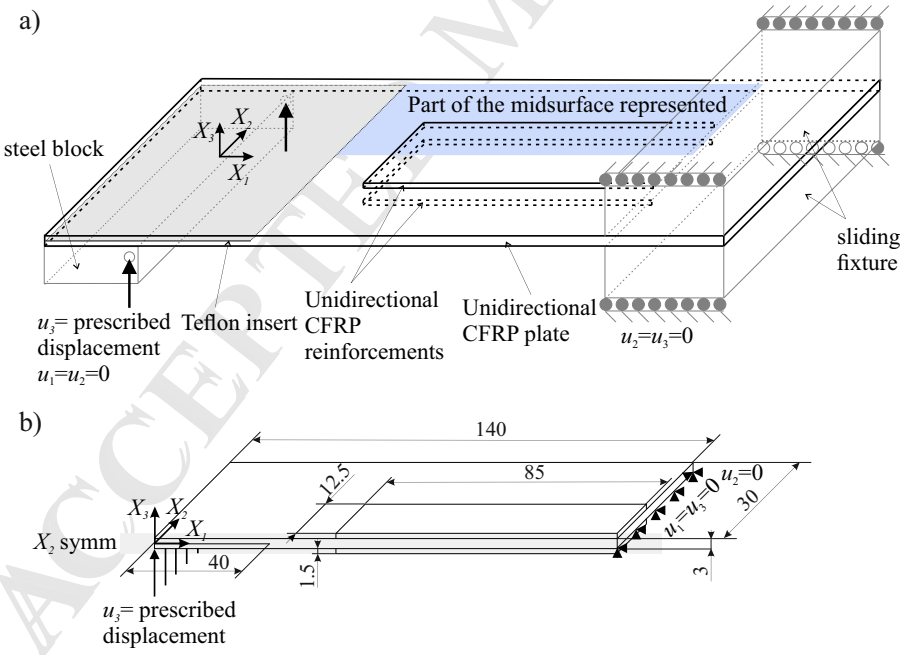

Figure 11: a) Sketch of the partially reinforced ELS specimen. The grey-shadowed area represents the Teflon insert. The blue-shadowed area is the area represented in figures 12.b, 13 and 18. b) Simplified model for FE simulation and dimensions (units in mm).

The historical evolution of the 0.5-valued damage isoline is plotted in Figure 12.a. The energy-

ACCEPTED MANUSCRIPT

Laminate properties			Interface properties		
E_{11}: Longitudinal Young's modulus	154	GPa	$\mathcal{G}_{Ic}$	0.3	N/mm
$E_{22} = E_{33}$: Transversal Young's modulus	8.5	GPa	$\mathcal{G}_{IIc}$	3	N/mm
$G_{12} = G_{13}$: Shear modulus in the longitudinal planes	4.2	GPa	τ_{Ic}	10	MPa
G_{23}: Shear modulus in the transversal plane	3.036	GPa	τ_{IIc}	31.62	MPa
$\mu_{12} = \mu_{13}$: Poison's coefficient in the longitudinal planes	0.35	-	η	2	-
μ_{23}: Poison's coefficient in the transversal plane	0.4	-	K	1E5	N/mm^3

Table 4: Laminate and interface properties used in the simulation study of Section 4. The nomenclature of the interface properties is defined in Appendix A.

based damage, $\mathcal{D}^e$, distribution is projected on the deformed midsurface, in Figure 12.c, for a prescribed displacement of 32.55 mm. Only the blue-shadowed area in Figure 11 is represented. The crack growth direction is evaluated at each integration point within the FPZ using criteria 1, 2 and 3, and represented in Figure 13. Note that criteria 1 (Figure 13.a) and 2 (Figure 13.b) are coincident except from at the elastic region, where no results from Criterion 1 can be obtained. By comparison of figures 13.b and 13.c, it can be observed that Criterion 3 only differs from criteria 1 and 2 at a region located at the upper left part of the cohesive zone ($X_1 < 85$ mm and $X_2 > 10$ mm). Indeed, the mode-mixity, B, is constant and equal to 1 in the entire cohesive zone, except for this region, where it locally decreases to 0.6 (see Figure 13.d). As demonstrated in Section 3, under constant B conditions, the growth driving direction is only governed by the kinematics of the cohesive elements. Therefore, evaluating any of the three criteria results in the same growth driving direction solution. On the other hand, only criteria 1 and 2 are affected by changes in the mode-dependent constitutive law, leading to different results, if compared to Criterion 3, at the region where the mode-mixity, B, varies.

In addition, four damage isolines have been traced. The damage isolines are constructed by connecting integration points with the same damage value. The first damage isoline, represented in Figure 14.a, is the line connecting the completely damaged integration points adjacent to the damage process zone. At each point on the damage isoline, the geometrical normal direction has been approximated by the normal to the slope of a second degree polynomial expression fitted to five consecutive points represented in white in Figure 14.a): the current point and the two preceding and the two succeeding points. Therefore, the approximated normal direction is computed by post-processing global informa-

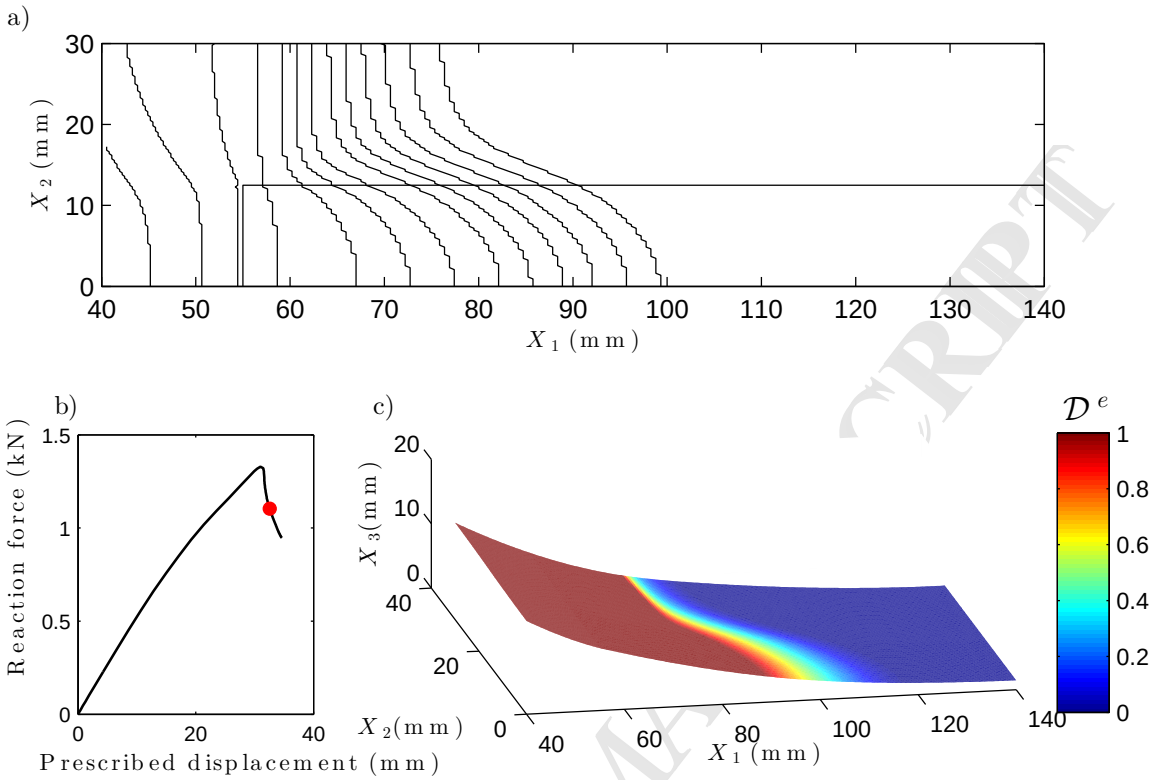

Figure 12: a) Historical evolution of the 0.5-valued damage isoline. b) Reaction force vs prescribed displacement curve with the current loading state highlighted in red. c) Energy-based damage projected on the deformed midsurface.

tion and it is heavily affected by the discretization and the choice of the fitting function. The results are compared to the local growth driving direction criteria developed in Section 2 in Figure 14.b. The same analysis is done with a 0.5-valued damage isoline (Figure 15), a 0.1-valued damage isoline (Figure 16) and the line connecting the undamaged integration points adjacent to the damage process zone (Figure 17). Note that, although for comparison purposes the growth driving direction is evaluated in a discrete manner at the same points where the approximated normal direction is computed, it is a continuous field that can be evaluated at any point, as shown in Figure 13.

Finally, three different FE models with element sizes 0.5 x 0.2 mm, 1 x 1.25 mm and 2.5 x 2.5 mm (see Figure 18) are used to compare the element size effect on both the approximated normal direction to the 1-valued damage isoline, evaluated by using global information, and the predicted growth driving direction using Criterion 1, evaluated point-wise at the element level. The results are

obtained using the information of the points on the 1-valued damage isoline traced in Figure 19 for the three meshes. The direction obtained along the damage isoline using both methods is plotted in Figure 20.

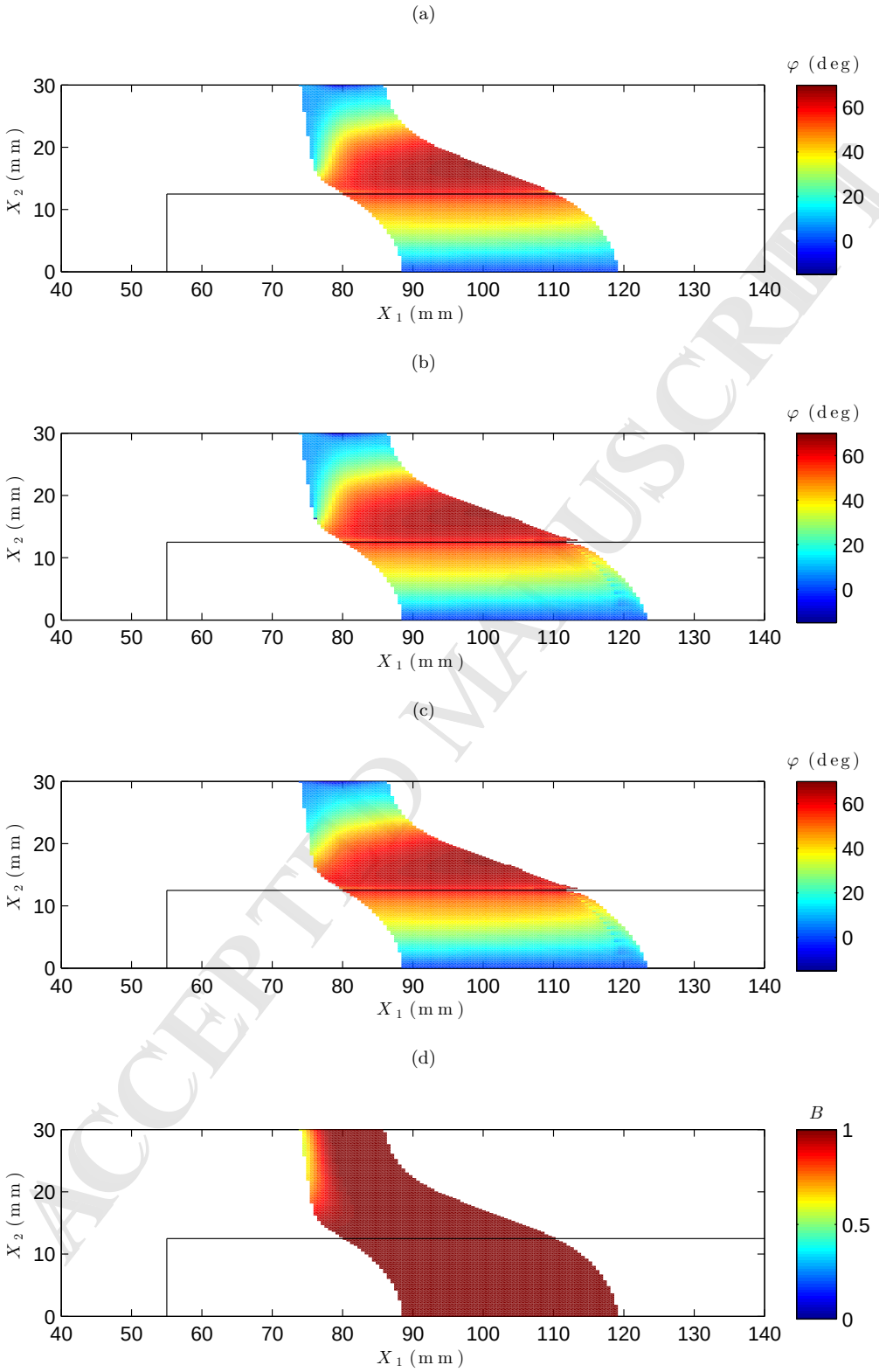

Figure 13: a) Growth driving direction resulting from the evaluation of Criterion 1. b) Growth driving direction resulting from the evaluation of Criterion 2. c) Growth driving direction resulting from the evaluation of Criterion 3. b) Mode mixity, B. The black line marks the reinforcements.

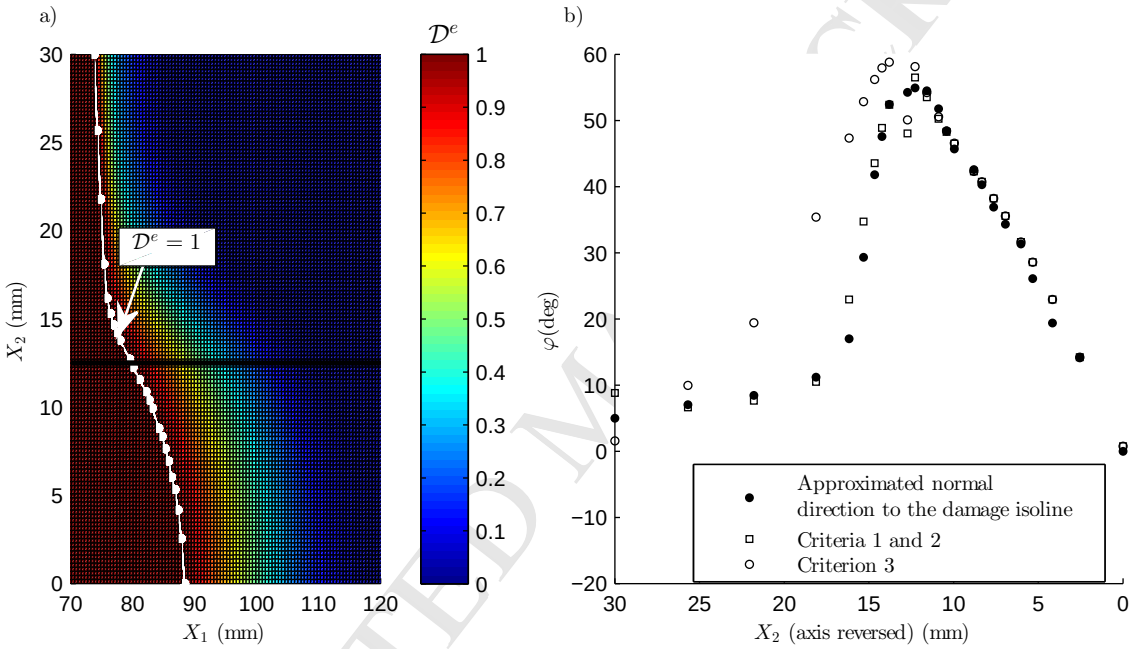

Figure 14: a) Energy-based damage, $\mathcal{D}^e$, distribution along the cohesive zone. The points forming the 1-valued damage isoline are highlighted in white. The thick black solid line marks the reinforcements border. b) Comparison of the angle φ obtained at the 1-valued damage front by computing the normal direction using global information and by locally evaluating the growth driving direction criteria. Criteria 1 and 2 are represented by the same marker because they lead to identical growth driving direction results.

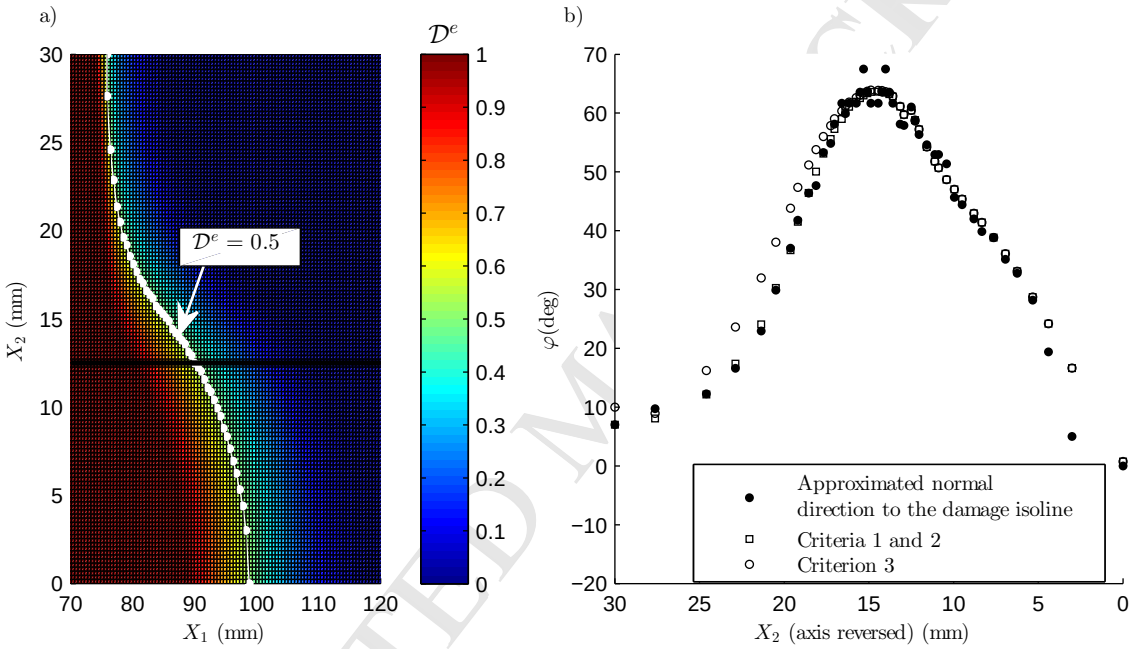

Figure 15: a) Energy-based damage, $\mathcal{D}^e$, distribution along the cohesive zone. The points forming the 0.5-valued damage isoline are highlighted in white. The thick black solid line marks the reinforcements border. b) Comparison of the angle φ obtained at the 0.5-valued damage front by computing the normal direction using global information and by locally evaluating the growth driving direction criteria. Criteria 1 and 2 are represented by the same marker because they lead to identical growth driving direction results.

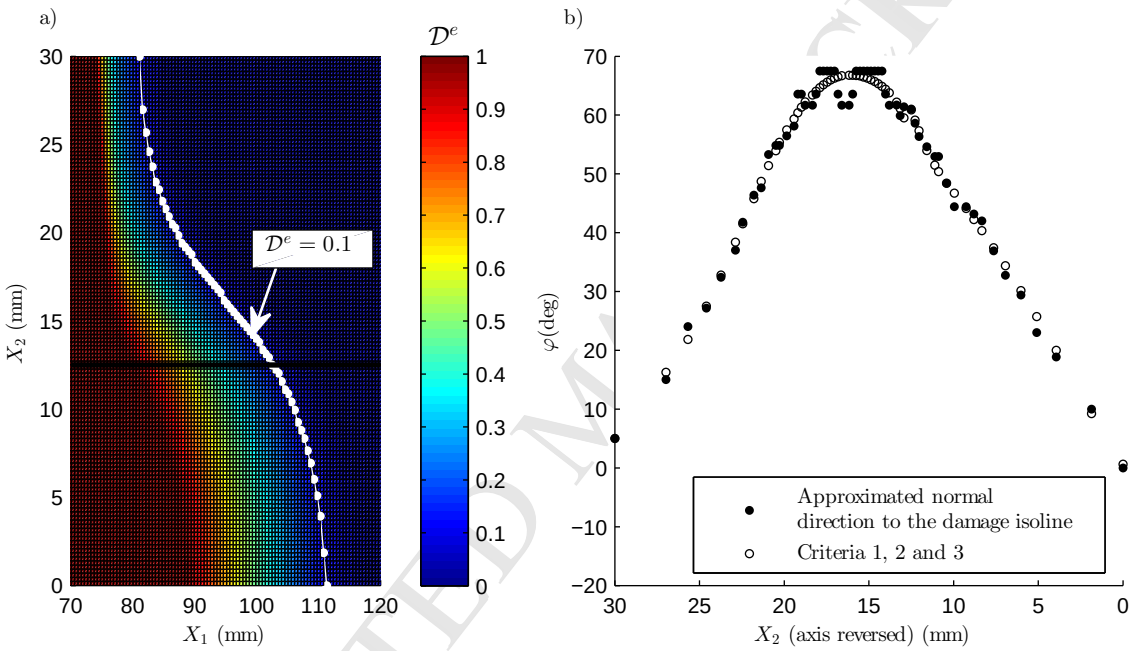

Figure 16: a) Energy-based damage, $\mathcal{D}^e$, distribution along the cohesive zone. The points forming the 0.1-valued damage isoline are highlighted in white. The thick black solid line marks the reinforcements border. b) Comparison of the angle φ obtained at the 0.1-valued damage front by computing the normal direction using global information and by locally evaluating the growth driving direction criteria. Criteria 1, 2 and 3 are represented by the same marker because they lead to identical growth driving direction results.

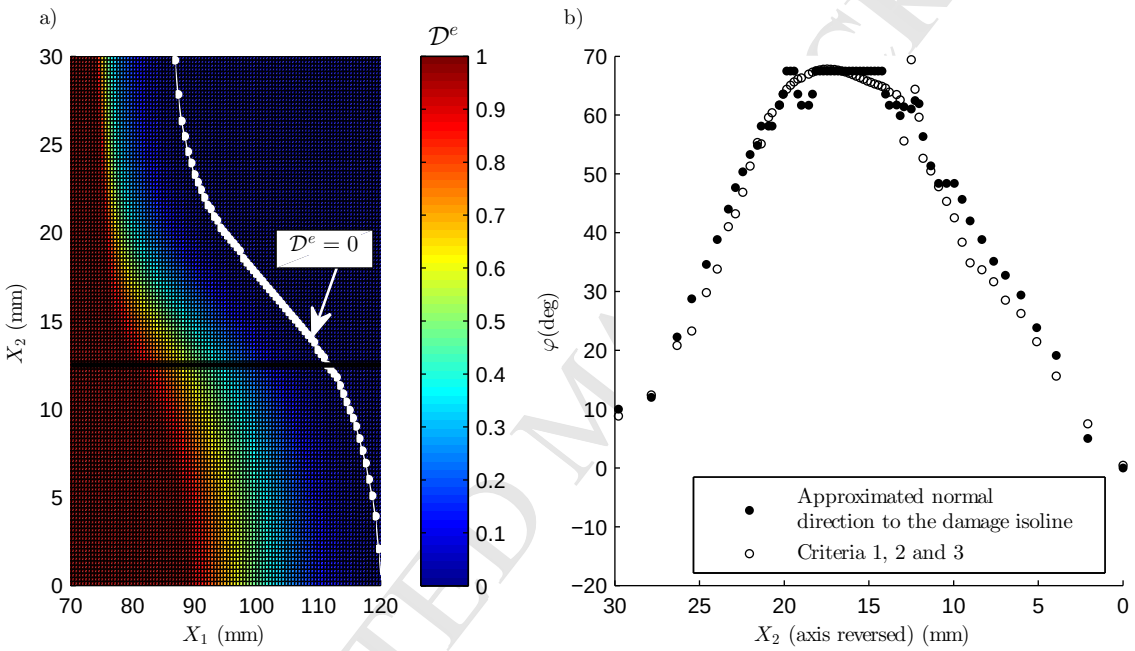

Figure 17: a) Energy-based damage, $\mathcal{D}^e$, distribution along the cohesive zone. The points forming the 0-valued damage isoline are highlighted in white. The thick black solid line marks the reinforcements border. b) Comparison of the angle φ obtained at the 0-valued damage front by computing the normal direction using global information and by locally evaluating the growth driving direction criteria. Criteria 1, 2 and 3 are represented by the same marker because they lead to identical growth driving direction results.

(a) Element size: 0.5 x 0.2 mmm

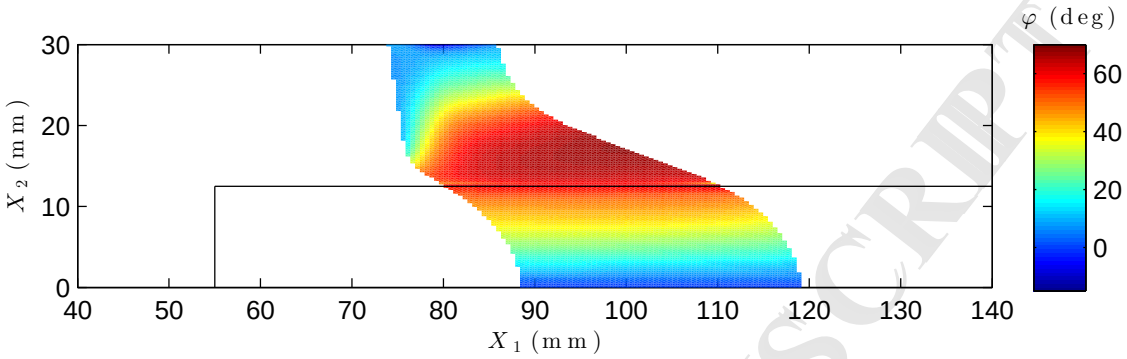

(b) Element size: 1 x 1.25 mmm

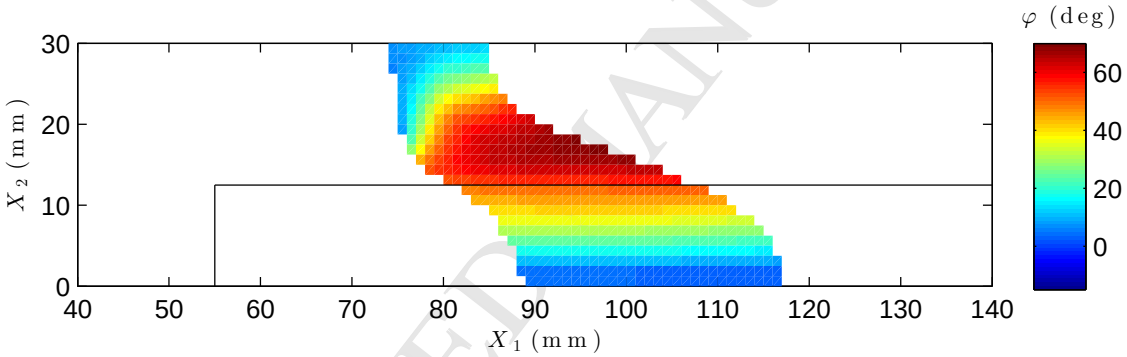

(c) Element size: 2.5 x 2.5 mmm

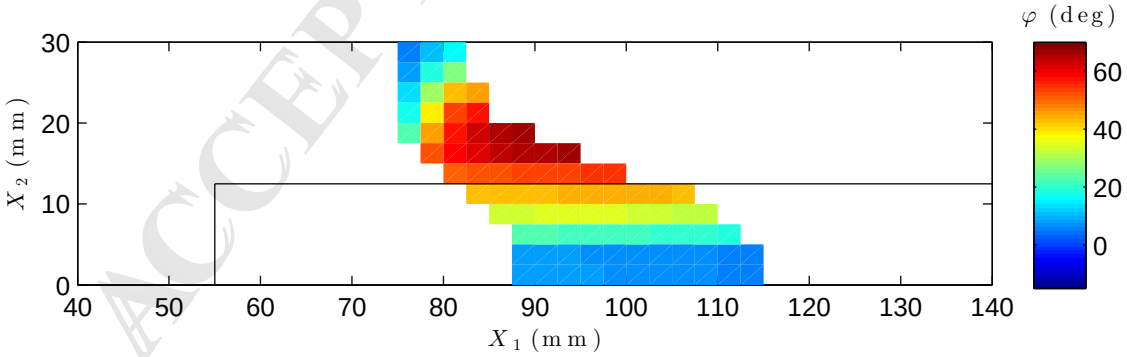

Figure 18: Growth driving direction resulting from the evaluation of Criterion 1 using three different element sizes.

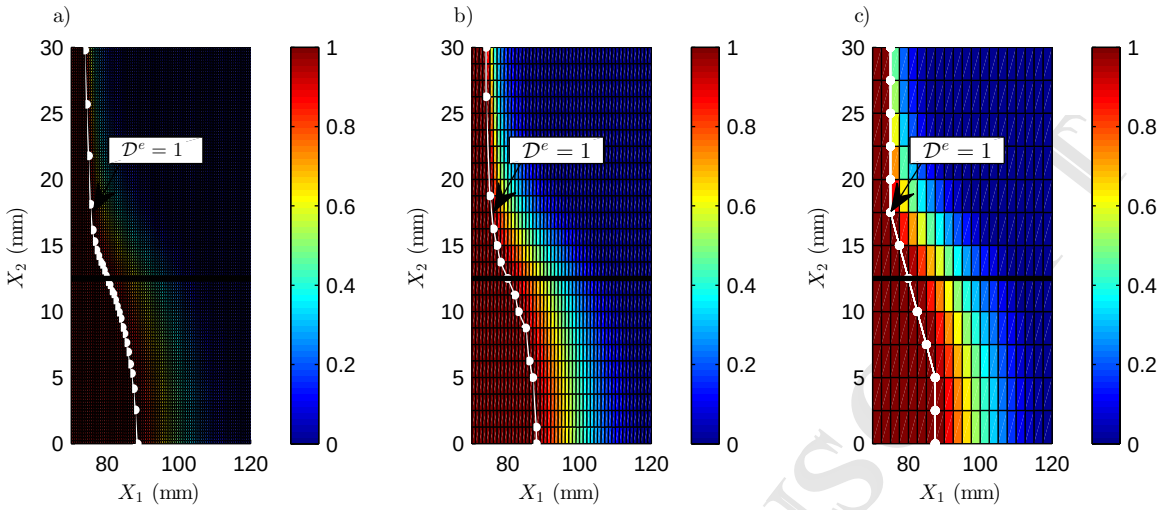

Figure 19: 1-valued damage fronts using different element sizes: a) 0.2 x 0.5 mm. b) 1 x 1.25 mm. c) 2.5 x 2.5 mm.

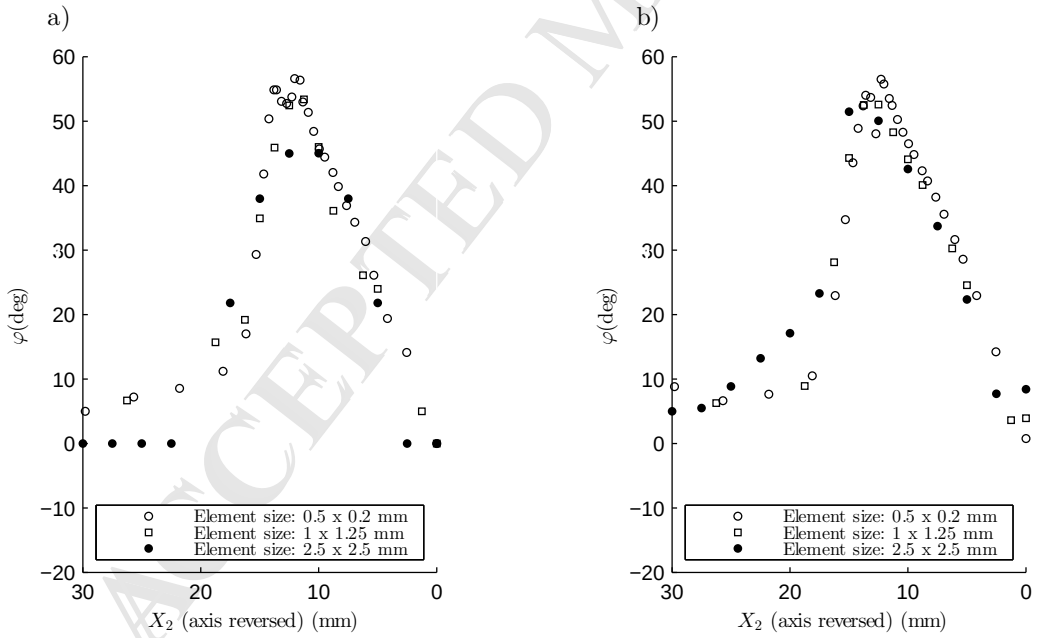

Figure 20: Comparison of the angle φ obtained at the 1-valued damage isoline using three different element sizes by a) computing the normal direction to the crack front using global information and b) evaluating Criterion 1.

ACCEPTED MANUSCRIPT

5. Discussion

Three different growth driving direction criteria have been proposed as element-level algorithms, that can be evaluated at any point within the cohesive zone. Criteria 1 and 2 are energetically-based formulations that account for both the kinematics and the constitutive law of the interface element. On the other hand, Criterion 3 is a geometrical approach, which only accounts for the kinematics of the interface element. Therefore, when the mode-mixity, B, is not constant, criteria 1 and 2 are the most appropriate. Moreover, Criterion 2 computes the rate of decrease of both the specific elastic energy, ω_e, and the dissipated energy, ω_d, normalized to the fracture toughness, $\mathcal{G}_c$. On the contrary, Criterion 1 only computes the rate of decrease of the dissipated energy, ω_d, normalized to the fracture toughness, $\mathcal{G}_c$, which is equivalent to computing the rate of decrease of the energy-based damage, $\mathcal{D}^e$. On this basis, Criterion 1 is not active before damage initiation, while Criterion 2 can be computed as soon as some separation between two initially coinciding points at the interface occurs. The three criteria have been presented for completeness, since they can be developed for other CZM formulations following the methodology described in Section 2.3. With the CZM used in this work, criteria 1 and 2 lead to the same growth driving direction solution at the damaged region. However, different results may be obtained if a mode-dependent penalty-stiffness is used, which could render the specific elastic energy of Crietion 2 dependent on growth driving direction.

The implementation of the formulation for the proposed growth driving direction criteria has been validated with one-element case studies in Section 3. The distribution of the quantities being analyzed have been projected on the element midsurface for visual verification (see figures 7-9 for different loading cases). In addition, the slopes of such quantities have been numerically evaluated at different orientations around a given evaluation point under Case C loading conditions (Figure 10). The orientation that results in lowest slopes coincides with the angle of growth driving direction predicted by each criteria, respectively.

Finally, the capabilities of the presented formulation are demonstrated in Section 4 using a three-dimensional run-out specimen loaded under ELS test conditions (Figure 11). The crack front propa-

ACCEPTED MANUSCRIPT

gates with non-straight shape due to the reinforcements bonded at the middle width of the specimen Figure 12. The growth driving direction criteria are evaluated at all the integration points within the cohesive zone for a given loading state with large deformations (Figure 13). The results from the three criteria differ only at those regions where the mode-mixity, B, is not constant, as already demonstrated in Section 3. Moreover, the resulting crack growth driving direction is compared with the geometrical normal direction of four different damage isolines computed by post-processing global information (figures 14-17). Both results are in good agreement, although the agreement is higher between the geometrical normal direction to the damage isolines derived from global information and the results from criteria 1 and 2, than from Criterion 3, specially at the non-constant mode-mixity, B, region. It is noteworthy that the global description of the damage isoline is highly dependent on the methodology used to compute it, mainly the number of points taken into account and its fitting. Therefore, in a FE framework, the computation of the approximated normal direction to the damage isoline using global information may, in some cases, misrepresent the actual normal direction. Indeed, the local computation of the negative gradient of the energy-based damage, $\mathcal{D}^e$, by means of Criterion 1 is the exact normal to the damage isolines. The fitting of the points forming the damage isoline, that leads to an approximate global description of it, is only used to validate the implementation of the formulation presented. To close, the effect of the mesh size on the determination of the normal direction to the 1-valued damage isoline is analyzed using both methods (Figure 20): the approximated normal direction using global information and the growth driving direction obtained by evaluating Criterion 1. The results show that the growth driving direction, evaluated locally, shows less sensitivity to the element size. Indeed, the growth driving direction is a continuum field which does not explicitly depend on the mesh size, but it implicitly does, due to discretization of the displacement field in the FEM [28].

ACCEPTED MANUSCRIPT

6. Conclusions

A novel method has been proposed for the determination of the growth driving direction for cohesive zone models. The presented formulation is evaluated point-wise. Therefore, it can be implemented as a part of a user-defined cohesive element subroutine and evaluated during simulation without the need of any extra loop, post-processing or global information.

The growth driving direction is defined as the negative gradient of the energy-based damage variable. However, other quantities can be used for the sake of simplicity. In this work, three different criteria are proposed. The implementation of the formulation for the proposed criteria applied to a particular CZM [15, 17] is derived and validated by using one-element analysis under different loading conditions.

Finally, the usefulness of the method has been demonstrated via the analysis of delamination propagation in a three-dimensional structure with a complex shaped crack front. The results using the proposed point-wise formulation for the evaluation of the growth driving direction are in agreement with the results from a global approximation of the normal direction to different damage isolines. Apart from being a low computational time-consuming task, the proposed formulation has the advantage that it can be evaluated at any point within the cohesive zone.

7. Acknowledgements

This work has been partially funded by the Spanish Government (Ministerio de Economia y Competitividad) under contract TRA2015-71491-R, cofinanced by the European Social Fund.

[1] R. Krueger, The virtual crack closure technique for modeling interlaminar failure and delamination in advanced composite materials, in: Numerical Modelling of Failure in Advanced Composite Materials, Woodhead Publishing Series in Composites Science and Engineering, 2015, pp. 3–53.

[2] FRANC3D, FRANC3D Concepts and User Guide - Version 2.6, Cornell Fracture Group, Ithaca, New York.

ACCEPTED MANUSCRIPT

[3] M. Schollmann, M. Fulland, H. Richard, Development of a new software for adaptive crack growth simulations in 3D structures, Engineering Fracture Mechanics 70 (2003) 249–268. doi:10.1016/S0013-7944(02)00028-0.

[4] E. Iesulauro, FRANC2D/L: A Crack Propagation Simulator for Plane Layered Structures - Version 1.5 User's Guide., Cornell Fracture Group, Ithaca, New York.

[5] D. Xie, S. B. Biggers Jr, Strain energy release rate calculation for a moving delamination front of arbitrary shape based on the virtual crack closure technique . Part I : Formulation and validation, Engineering Fracture Mechanics 73 (2006) 771–785. doi:10.1016/j.engfracmech.2005.07.013.

[6] X. Li, C. Ferrie, E. Nottorf, M. Portanova, Virtual crack closure technique on stepped crack front (VCCT-S), Annual Forum Proceedings - American Helicopter Society 64 (2).

[7] Y.-P. Liu, C.-Y. Chen, G.-Q. Li, A modified zigzag approach to approximate moving crack front with arbitrary shape, Engineering Fracture Mechanics 78 (2) (2011) 234–251. doi:10.1016/j.engfracmech.2010.08.007.

[8] D. Dugdale, Yielding of steel sheets containing slits, Journal of the Mechanics and Physics of Solids 8 (2) (1960) 100–104. doi:10.1016/0022-5096(60)90013-2.

[9] G. Barenblatt, The Mathematical Theory of Equilibrium Cracks in Brittle Fracture, Advances in Applied Mechanics 7 (1962) 55–129. doi:10.1016/S0065-2156(08)70121-2.

[10] J. L. Chaboche, R. Girard, A. Schaff, Numerical analysis of composite systems by using interphase / interface models, Computational Mechanics 20 (1-2). doi:10.1007/s004660050209.

[11] M. Ortiz, A. Pandolfi, Finite-Deformation Irreversible Cohesive Elements for Three-Dimensional Crack-Propagation Analysis, International Journal for Numerical Methods in EngineeringI 44 (1999) 1267–1282. doi:10.1002/(SICI)1097-0207(19990330)44:9¡1267::AID-NME486¿3.0.CO;2-7.

ACCEPTED MANUSCRIPT

[12] G. Alfano, M. A. Crisÿeld, Finite element interface models for the delamination analysis of laminated composites: mechanical and computational issues, International Journal for Numerical Methods in Engineering 50 (2001) 1701–1736. doi:10.1002/nme.93.

[13] P. P. Camanho, C. Davila, M. de Moura, Numerical simulation of mixed-mode progressive delamination in composite materials, Journal of Composite Materials 37 (16) (2003) 1415–1438. doi:10.1177/0021998303034505.

[14] V. K. Goyal, E. R. Johnson, G. D. Carlos, Irreversible constitutive law for modeling the delamination process using interfacial surface discontinuities, Composite Structures 65 (2004) 289–305. doi:10.1016/j.compstruct.2003.11.005.

[15] A. Turon, P. P. Camanho, J. Costa, C. G. Da, A damage model for the simulation of delamination in advanced composites under variable-mode loading, Mechanics of Materials 38 (2006) 1072–1089. doi:10.1016/j.mechmat.2005.10.003.

[16] W.-G. Jiang, S. R. Hallett, B. G. Green, M. R. Wisnom, A concise interface constitutive law for analysis of delamination and splitting in composite materials and its application to scaled notched tensile specimens, International Journal for Numerical Methods in Engineering 69 (2007) 1982–1995. doi:10.1002/nme.

[17] A. Turon, P. P. Camanho, J. Costa, J. Renart, Accurate simulation of delamination growth under mixed-mode loading using cohesive elements: Definition of interlaminar strengths and elastic stiffness, Composite Structures 92 (8) (2010) 1857–1864. doi:10.1016/j.compstruct.2010.01.012.

[18] B. L. V. Bak, C. Sarrado, A. Turon, J. Costa, Delamination Under Fatigue Loads in Composite Laminates: A Review on the Observed Phenomenology and Computational Methods, Applied Mechanics Reviews 66 (6).

[19] L. F. Kawashita, S. R. Hallett, A crack tip tracking algorithm for cohesive interface element

ACCEPTED MANUSCRIPT

analysis of fatigue delamination propagation in composite materials, International Journal of Solids and Structures 49 (21) (2012) 2898–2913. doi:10.1016/j.ijsolstr.2012.03.034.

[20] C. Wang, X. Xu, Cohesive element analysis of fatigue delamination propagation in composite materials with improved crack tip tracking algorism, Composite Structures 134 (2015) 176–184. doi:10.1016/j.compstruct.2015.07.118.

[21] B. L. V. Bak, A. Turon, E. Lindgaard, E. Lund, A simulation method for high-cycle fatigue-driven delamination using a cohesive zone model, International Journal for Numerical Methods in Engineering 106 (2016) 163–191. doi:10.1002/nme.5117.

[22] B. L. V. Bak, A. Turon, E. Lindgaard, E. Lund, A benchmark study of simulation methods for high-cycle fatigue-driven delamination based on cohesive zone models, Composite structures 164 (2017) 198–206.

[23] F. P. van Der Meer, N. Moës, L. J. Sluys, A level set model for delamination Modeling crack growth without cohesive zone or stress singularity, Engineering Fracture Mechanics 79 (2012) 191–212. doi:10.1016/j.engfracmech.2011.10.013.

[24] F. P. van der Meer, L. J. Sluys, The Thick Level Set method : Sliding deformations and damage initiation, Comput. Methods Appl. Mech. Engrg. 285 (2015) 64–82. doi:10.1016/j.cma.2014.10.020.

[25] M. L. Benzeggagh, M. Kenane, Measurement of Mixed-Mode Delamination Fracture Toughness of Unidirectional Glass/ Epoxy Composites with Mixed-ModeE Bending Apparatus, Composite Science and Technology 56 (1996) 439–449. doi:10.1016/S0266-3538(97)00021-3.

[26] A. Turon, E. Gonzalez, C. Sarrado, G. Guillamet, P. Maimi, Accurate simulation of delamination under mixed-mode loading using a cohesive model with a mode-dependent penalty stiffness, Composite Structures 184 (2018) 506–511.

[27] D. Systémes, Abaqus manual 6.12.

[28] B. L. V. Bak, E. Lindgaard, E. Lund, International Journal for Numerical Methods in Engineering.

ACCEPTED MANUSCRIPT

Appendix A. The cohesive element formulation

The cohesive zone model from the original work of Turon et al. [15, 17] and its finite element implementation are outlined in the following.

Appendix A.1. Kinematics

Let the delamination be understood as a strong discontinuous singular surface, S, that crosses a volume of material, Ω, and divides it into two subdomains, Ω^+ and Ω^-, as shown in Figure A.21. There are two surfaces that bound into S: the upper surface, S^+, associated with Ω^+, and the lower surface, S^-, associated with Ω^-. These two surfaces, which are initially coincident with the reference surface, S^0, in the undeformed configuration, represent the crack faces. They independently translate, rotate and stretch, though their motion is constrained by the constitutive law used to describe the interface.

The reference surface, S^0, is defined in a the three-dimensional space, as shown in Figure A.22, by the global Cartesian coordinates X_i, where $i = 1, 2, 3$. Conveniently, the internal deformed middle surface, $\overline{S}$, can be defined, through the history of deformations, as the average distance between two initially coinciding points,

$$\overline{x}_i = X_i + \frac{1}{2}\left(u_i^+ + u_i^-\right) \tag{A.1}$$

where $u_i^{\pm}$ are the displacements of the two material points on $S^{\pm}$ that are related to the point X_i, contained in S^0. Hence, defining a local Cartesian coordinate system $(\hat{\boldsymbol{e}}_1, \hat{\boldsymbol{e}}_2, \hat{\boldsymbol{e}}_3)$ on $\overline{S}$, the normal and tangential components of the displacement jump across the material discontinuity can be expressed according to the local orientation of the midsurface.

Let η_1 and η_2 be curvilinear coordinates located on $\overline{S}$, as represented in Figure A.22 (Note that the isoparametric representation of the physical space is reduced to the interfacial element midsurface). Then, two vectors tangential to the deformed midsurface are established as:

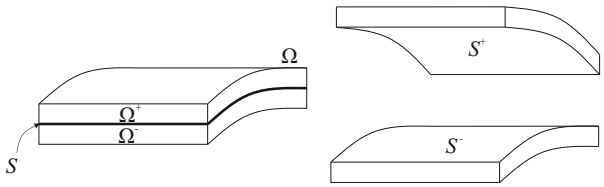

Figure A.21: Interfacial surface, S, traversing a body, Ω, and diving it into Ω^+ and Ω^- subdomains. The exploded view shows the upper S^+ and lower S^- surfaces that bound into S.

$$\boldsymbol{e'_1} = \frac{\partial \overline{x}_i}{\partial \eta_1} \qquad \boldsymbol{e'_2} = \frac{\partial \overline{x}_i}{\partial \eta_2} \tag{A.2}$$

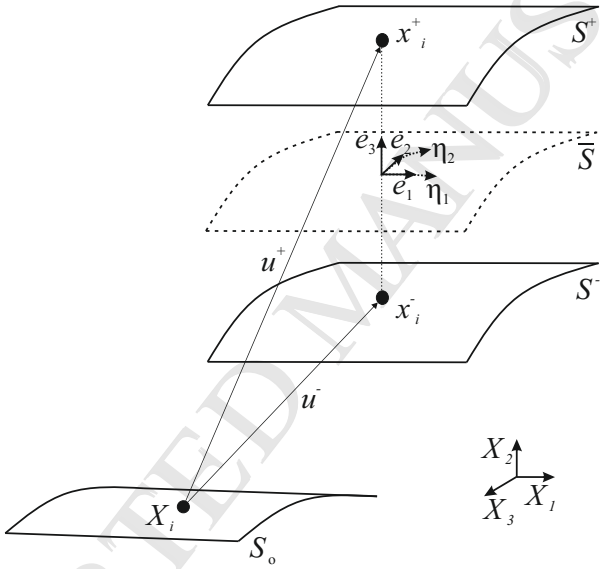

Figure A.22: Description of the deformed element midsurface, $\overline{S}$.

The direction cosines of the local Cartesian coordinate system, are the normal, $\hat{\boldsymbol{e}}_3$, and tangential, $\hat{\boldsymbol{e}}_1$ and $\hat{\boldsymbol{e}}_2$, unit vectors to $\overline{S}$, and can be derived from the Equation (A.2) as follows:

$$\hat{\boldsymbol{e}}_1 = \frac{\boldsymbol{e'_1}}{|\boldsymbol{e'_1}|} \qquad \hat{\boldsymbol{e}}_3 = \frac{\boldsymbol{e'_1} \times \boldsymbol{e'_2}}{|\boldsymbol{e'_1} \times \boldsymbol{e'_2}|} \qquad \hat{\boldsymbol{e}}_2 = \hat{\boldsymbol{e}}_3 \times \hat{\boldsymbol{e}}_1 \tag{A.3}$$

Finally, the displacement jump in local coordinates can be expressed in terms of the displacement field:

$$\delta_j = \Theta_{ji}\left(u_i^+ - u_i^-\right), \qquad i,j = 1,2,3 \tag{A.4}$$

where $\left(u_i^+ - u_i^-\right)$ is the separation of two initially coinciding points at the interface in the global Cartesian coordinate system, and Θ_{ji} is the transformation tensor that relates the global to the local coordinate system,

$$\boldsymbol{\Theta} = [\hat{\boldsymbol{e}}_1, \hat{\boldsymbol{e}}_2, \hat{\boldsymbol{e}}_3]^T \tag{A.5}$$

Appendix A.2. Constitutive model

The constitutive relation between the displacement jumps, δ_j, and the tractions between crack faces, τ_j, is defined as

$$\begin{aligned} \tau_j &= \left(1 - \mathcal{D}^K\right) K \delta_j \qquad \text{for} \qquad j = 1,2 \\ \tau_3 &= \left(1 - \mathcal{D}^K\right) K \delta_3 - \mathcal{D}^K K \langle -\delta_3 \rangle \end{aligned} \tag{A.6}$$

where $\mathcal{D}^K \in [0,1]$ is a scalar damage parameter reducing the initial constitutive tangent stiffness, K and $\langle\ \rangle$ are the Macaulay brackets defined as $\langle x \rangle = (x + |x|)$. Note that, as interpenetration of crack faces is physically prevented by contact, negative normal opening values are avoided.

The evolution of the stiffness degrading damage variable, $\mathcal{D}^K$ is governed by an equivalent one-dimensional cohesive law and a damage criterion. For the formulation of this equivalent one-dimensional cohesive law, and so that different stages of the degrading process can be compared under changing mixed-mode loading conditions, a non-negative scalar displacement jump is defined:

$$\lambda = \sqrt{(\delta_I)^2 + (\delta_s)^2} \tag{A.7}$$

where δ_I is the mode I opening, associated to the displacement jump in the normal direction to the

ACCEPTED MANUSCRIPT

midsurface, and δ_s is the shear sliding resulting of the displacement jumps in the tangential directions to the midsurface.

$$\delta_I = \langle \delta_3 \rangle, \qquad \delta_s = \sqrt{(\delta_1)^2 + (\delta_2)^2} \tag{A.8}$$

Note that the two tangential (orthogonal among each other) displacement jumps, δ_1 and δ_2, are reduced to an equivalent shear displacement jump, δ_s. It is worth to mention that this is due to the incapability of the original formulation [15, 17] to distinguish into modes II and III, mainly attributed to the hitherto lack of computationally-efficient crack front tracking algorithms, and not supported by any physical evidence. In any event, shear opening mode is, conservatively, treated as mode II in the present constitutive model.

The equivalent one-dimensional interface traction is related to the equivalent one-dimensional displacement jump with

$$\mu = \left(1 - \mathcal{D}^K\right) K \lambda \tag{A.9}$$

With increasing displacement jump, the traction increases to a peak value, μ_o, corresponding to the interfacial strength, and then decreases until complete decohesion. To ensure the correct energy dissipation during the process of fracture, the total area under the traction-displacement jump curve is set equal to the fracture toughness, $\mathcal{G}_c$. Both the interfacial strength and the fracture toughness are material parameters that depend on the opening mode-mixity, and, together with the penalty stiffness, K, define the shape of the constitutive law.

The local mode-mixity, B, is defined in terms of the displacement jump as:

$$B = \frac{\delta_s^2}{\delta_I^2 + \delta_s^2} \tag{A.10}$$

and it is equivalent to the amount of total specific work related to shear mode over the entire total

ACCEPTED MANUSCRIPT

specific work (the reader is referred to Figure 2 for an schematic representation of the total specific work of the interface).

The critical energy release rate, $\mathcal{G}_c$, for a given mode-mixity is determined using the expression proposed in [25],

$$\mathcal{G}_c = \mathcal{G}_{Ic} + (\mathcal{G}_{IIc} - \mathcal{G}_{Ic})\, B^{\eta} \tag{A.11}$$

where subscripts I and II denote the pure modes I and II values, respectively, and η is an experimentally determined mode interaction parameter. Similarly, the interfacial strength, μ_o, for a given mode-mixity is defined as

$$\mu_o = \sqrt{(\tau_{Io})^2 + [(\tau_{IIo} - \tau_{Io})]\, B^{\eta}} \tag{A.12}$$

In terms of the displacement jump, the onset, λ_o, and propagation, λ_c, of delamination are related to the parameters of the cohesive law:

$$\lambda_o = \frac{\mu_o}{K}, \qquad \lambda_c = \frac{2\mathcal{G}_c}{\mu_o} \tag{A.13}$$

The damage criterion is formulated ensuring damage irreversibility, such that the damage variable at the current time t_c determined as

$$\mathcal{D}^K = \min\left(\max\left(0, \frac{\lambda_c^t\,(\lambda^t - \lambda_o^t)}{\lambda^t\,(\lambda_c^t - \lambda_o^t)}\right), 1\right) \qquad \forall\ t \in [0, t_c] \tag{A.14}$$

Thus, the mixed-mode displacement jump associated to the current damage state is

$$\lambda_{\mathcal{D}} = \frac{\lambda_o \lambda_c}{\lambda_c - \mathcal{D}^K\,(\lambda_c - \lambda_o)} \tag{A.15}$$

The stiffness degrading damage variable, $\mathcal{D}^K$, is strongly nonlinear in terms of $\lambda_{\mathcal{D}}$. This might hinder the performance of the numerical method [21]. Conversely, an energy-based damage variable,

ACCEPTED MANUSCRIPT

which exhibits linear dependency with $\lambda_{\mathcal{D}}$, is defined in [17] and [21] as the specific dissipated energy due to fracture over the fracture toughness during degradation ($\lambda_o < \lambda_{\mathcal{D}} < \lambda_c$):

$$\begin{cases} \mathcal{D}^e = 0 & \text{for} \quad \lambda_{\mathcal{D}} \leq \lambda_o \\ \mathcal{D}^e = \dfrac{\omega_d}{\mathcal{G}_c} & \text{for} \quad \lambda_o \leq \lambda_{\mathcal{D}} \leq \lambda_c \\ \mathcal{D}^e = 1 & \text{for} \quad \lambda_{\mathcal{D}} \geq \lambda_c \end{cases} \tag{A.16}$$

where ω_d is, in terms of the displacement jump is given as:

$$\omega_d = \max\left\{0, \frac{1}{2} K \lambda_o \lambda_c \frac{\lambda_o - \lambda_{\mathcal{D}}}{\lambda_o - \lambda_c}\right\} \tag{A.17}$$

Finally, the total specific work associated to the current damage state can also be determined in terms of the displacement jump:

$$\omega_{tot} = \frac{1}{2} K \lambda_o \left(\lambda_c - \frac{(\lambda_c - \lambda_{\mathcal{D}})^2}{\lambda_c - \lambda_o}\right) \tag{A.18}$$

Note that, during crack propagation, the μ-λ relation follows the equivalent one-dimensional cohesive law, i.e.:

$$\lambda_{\mathcal{D}} = \lambda \tag{A.19}$$

and that before damage initiation, the no energy is dissipated yet and the total specific work corresponds to the specific elastic energy:

$$\omega_{tot} = \frac{1}{2} K \lambda^2 \tag{A.20}$$

Appendix A.3. Finite element implementation

The three dimensional crack propagation problem is discretized here using the FE method. The cohesive interface is implemented into an eight-noded zero-thickness element. This interface element

ACCEPTED MANUSCRIPT

is compatible with three dimensional continuum elements that may form the upper and lower part of the body containing the singularity.

The nodal coordinates of the undeformed interface element are arranged in vector $\boldsymbol{C}$ in such a way that:

$$\boldsymbol{C} = \left\{\boldsymbol{C}^{-}, \boldsymbol{C}^{+}\right\} \tag{A.21}$$

being $C_k^- = \left\{X_1^1, X_2^1, X_3^1, ..., X_1^4, X_2^4, X_3^4\right\}^T$ and $C_k^+ = \left\{X_1^5, X_2^5, X_3^5, ..., X_1^8, X_2^8, X_3^8\right\}^T$ the global coordinates of the nodes at the lower and upper interfaces, respectively, where X_i^n is the i-th coordinate of the n-th node.

The nodal displacements, relative to the global coordinates, are arranged in vector $\boldsymbol{Q}$ similarly to the nodal coordinates, i.e. the nodal displacements of the lower interface, $Q_k^- = \left\{u_1^1, u_2^1, u_3^1, ..., u_1^4, u_2^4, u_3^4\right\}^T$, are numbered first, and the nodal displacements of the upper interface, $Q_k^+ = \left\{u_1^5, u_2^5, u_3^5, ..., u_1^8, u_2^8, u_3^8\right\}^T$, are numbered second,

$$\boldsymbol{Q} = \left\{\boldsymbol{Q}^{-}, \boldsymbol{Q}^{+}\right\} \tag{A.22}$$

The material coordinates and the displacement field are interpolated within the domain of the surface element using isoparametric bilinear shape functions,

$$\begin{aligned} L_1 &= \frac{1}{2}\left(1-\eta_1\right)\left(1-\eta_2\right); \qquad L_2 = \frac{1}{2}\left(1+\eta_1\right)\left(1-\eta_2\right) \\ L_3 &= \frac{1}{2}\left(1+\eta_1\right)\left(1+\eta_2\right); \qquad L_4 = \frac{1}{2}\left(1-\eta_1\right)\left(1+\eta_2\right) \end{aligned} \tag{A.23}$$

organized in matrix the shape function matrix, N_{ik}, as follows:

ACCEPTED MANUSCRIPT

$$N_{ik} = \begin{bmatrix} L_1 & 0 & 0 & L_2 & 0 & 0 & L_3 & 0 & 0 & L_4 & 0 & 0 \\ 0 & L_1 & 0 & 0 & L_2 & 0 & 0 & L_3 & 0 & 0 & L_4 & 0 \\ 0 & 0 & L_1 & 0 & 0 & L_2 & 0 & 0 & L_3 & 0 & 0 & L_4 \end{bmatrix} \tag{A.24}$$

According to Equation (A.1) and making use of equations (A.21)-(A.24), the coordinates of the interfacial deformed midsurface are:

$$\overline{x}_i = \frac{1}{2} N_{ik} \left(C_k^+ + C_k^- + Q_k^+ + Q_k^- \right) \tag{A.25}$$

The tangential vectors to the interfacial midsurface at (η_1, η_2), defined in Equation (A.2), are now arranged in the Jacobian matrix,

$$\boldsymbol{J} = [\boldsymbol{e}_1', \boldsymbol{e}_2'] \qquad \text{where} \qquad J_{i\alpha} = \frac{1}{2} \frac{\partial N_{ik}}{\partial \eta_\alpha} \left(C_k^+ + C_k^- + Q_k^+ + Q_k^- \right) \tag{A.26}$$

where the subscript $\alpha = 1, 2$.

Hence, the unit vectors, $\hat{\boldsymbol{e}}_1$, $\hat{\boldsymbol{e}}_2$, $\hat{\boldsymbol{e}}_3$, corresponding to the direction cosines of the local Cartesian coordinate system, can be derived from $J_{i\alpha}$ following equation (A.3).

Finally, the transformation matrix, M_{im}, computes the displacement jump in global coordinates of two initially coinciding points from the nodal global displacement vector:

$$u_i^+ - u_i^- = M_{im} Q_m \tag{A.27}$$

where subscript m runs form 1 to the number of degrees of freedom of the element ($m = 1...24$) and M_{im} is defined as:

$$M_{im} = [-N_{ik} \; N_{ik}] \tag{A.28}$$

Thus, from Equation (A.4), the displacement jump in local coordinates reads:

ACCEPTED MANUSCRIPT

$$\delta_j = \Theta_{ji} M_{im} Q_m \tag{A.29}$$

For the sake of simplicity, only the derivation of the displacement jump field is depicted above, as the only field needed for the resolution of the criteria presented in section 2.2. See [15] for the derivation of the interface element tangent stiffness matrix, $\boldsymbol{K}$, and internal force vector, ${}^{int}\boldsymbol{f}$ required in the nonlinear solution procedure.

Appendix B. Development of the criteria to determine the growth driving direction

The formulation of the three proposed criteria in section 2.2 to determine the growth driving direction is synthesized in Table B.5. The equations to solve for Criterion 1 are found by introducing equations (B.2) and (B.3) in equations (B.1) and (B.4) and computing the radial slopes of the mixed-mode displacement jump, $\frac{\partial \lambda}{\partial \rho}$, and mode-mixity, $\frac{\partial B}{\partial \rho}$. On the ohter hand, the equations for Criterion 2 are found by introducing equations (B.6) and (B.7) in equations (B.5) and (B.8). Also the radial slopes of the mixed-mode displacement jump, $\frac{\partial \lambda}{\partial \rho}$, and mode-mixity, $\frac{\partial B}{\partial \rho}$, are required. Finally, for the evaluation of Criterion 3 only the slope of the mixed-mode displacement jump in the radial direction, $\frac{\partial \lambda}{\partial \rho}$, is needed (see equations (B.9) and (B.10)).

Moreover, in this work, the criteria are applied to the CZM presented in [15, 17] to exemplify their capabilities. In this particular case, the factors F_B and F_λ are reduced to equations (B.11) and (B.12), for Criterion 1, and reduced to equations (B.13) and (B.14), for Criterion 2. Equations (B.11) and (B.12) are obtained by introducing equations (B.15)-(B.24) into equations (B.2) and (B.3). Equations (B.13) and (B.14) are obtained by introducing equations (B.15)-(B.19) and (B.25)-(B.29) into equations (B.6) and (B.7). Also, the derivation of the radial slopes of the mixed-mode displacement jump and mode-mixity, $\frac{\partial \lambda}{\partial \rho}$ and $\frac{\partial B}{\partial \rho}$, after the particular application to the CZM from [15, 17] is detailed in section 2.3.

Criterion ID	Functions to solve		F_B		F_λ	
1	$\frac{\partial}{\partial\varphi}\frac{\partial\mathcal{D}^e}{\partial\rho} = \frac{\partial}{\partial\varphi}\left(F_B\frac{\partial B}{\partial\rho} + F_\lambda\frac{\partial\lambda}{\partial\rho}\right) = 0$	(B.1)	$\frac{\partial\left(\frac{\omega_d}{\mathcal{G}_c}\right)}{\partial\omega_d}\left(\frac{\partial\omega_d}{\partial\lambda_o}\frac{\partial\lambda_o}{\partial\mu_o} + \frac{\partial\omega_d}{\partial\lambda_c}\frac{\partial\lambda_c}{\partial\mu_o}\right)\frac{\partial\mu_o}{\partial B} +$	(B.2)	$\frac{\partial\left(\frac{\omega_d}{\mathcal{G}_c}\right)}{\partial\omega_d}\frac{\partial\omega_d}{\partial\lambda}$	(B.3)
	$\frac{\partial^2}{\partial\varphi^2}\frac{\partial\mathcal{D}^e}{\partial\rho} = \frac{\partial^2}{\partial\varphi^2}\left(F_B\frac{\partial B}{\partial\rho} + F_\lambda\frac{\partial\lambda}{\partial\rho}\right) > 0$	(B.4)	$+\left(\frac{\partial\left(\frac{\omega_d}{\mathcal{G}_c}\right)}{\partial\omega_d}\frac{\partial\omega_d}{\partial\lambda_c}\frac{\partial\lambda_c}{\partial\mathcal{G}_c} + \frac{\partial\left(\frac{\omega_d}{\mathcal{G}_c}\right)}{\partial\mathcal{G}_c}\right)\frac{\partial\mathcal{G}_c}{\partial B}$			
2	$\frac{\partial}{\partial\varphi}\frac{\partial\left(\frac{\omega_{tot}}{\mathcal{G}_c}\right)}{\partial\rho} = \frac{\partial}{\partial\varphi}\left(F_B\frac{\partial B}{\partial\rho} + F_\lambda\frac{\partial\lambda}{\partial\rho}\right) = 0$	(B.5)	$\frac{\partial\left(\frac{\omega_{tot}}{\mathcal{G}_c}\right)}{\partial\omega_{tot}}\left(\frac{\partial\omega_{tot}}{\partial\lambda_o}\frac{\partial\lambda_o}{\partial\mu_o} + \frac{\partial\omega_{tot}}{\partial\lambda_c}\frac{\partial\lambda_c}{\partial\mu_o}\right)\frac{\partial\mu_o}{\partial B} +$	(B.6)	$\frac{\partial\left(\frac{\omega_{tot}}{\mathcal{G}_c}\right)}{\partial\omega_{tot}}\frac{\partial\omega_{tot}}{\partial\lambda}$	(B.7)
	$\frac{\partial^2}{\partial\varphi^2}\frac{\partial\left(\frac{\omega_{tot}}{\mathcal{G}_c}\right)}{\partial\rho} = \frac{\partial^2}{\partial\varphi^2}\left(F_B\frac{\partial B}{\partial\rho} + F_\lambda\frac{\partial\lambda}{\partial\rho}\right) > 0$	(B.8)	$+\left(\frac{\partial\left(\frac{\omega_{tot}}{\mathcal{G}_c}\right)}{\partial\omega_{tot}}\frac{\partial\omega_{tot}}{\partial\lambda_c}\frac{\partial\lambda_c}{\partial\mathcal{G}_c} + \frac{\partial\left(\frac{\omega_{tot}}{\mathcal{G}_c}\right)}{\partial\mathcal{G}_c}\right)\frac{\partial\mathcal{G}_c}{\partial B}$			
3	$\frac{\partial}{\partial\varphi}\frac{\partial\lambda}{\partial\rho} = 0$	(B.9)	—		—	
	$\frac{\partial^2}{\partial\varphi^2}\frac{\partial\lambda}{\partial\rho} > 0$	(B.10)				

Table B.5: Equations to solve for each criteria to determine the growth driving direction, φ.

ACCEPTED MANUSCRIPT

ACCEPTED MANUSCRIPT

Criterion ID	F_B		F_λ	
1	$\dfrac{\eta\left(\mathcal{G}_{IIc}-\mathcal{G}_{Ic}\right)B^{(\eta-1)}\lambda}{K\lambda_c\lambda_o\left(\lambda_o-\lambda_c\right)}$	(B.11)	$\dfrac{1}{\lambda_c-\lambda_o}$	(B.12)
2	$\dfrac{2\eta\left(\mathcal{G}_{IIc}-\mathcal{G}_{Ic}\right)B^{(\eta-1)}\lambda\left(\lambda_c-\lambda\right)}{K\lambda_c^2\lambda_o\left(\lambda_o-\lambda_c\right)}$	(B.13)	$\dfrac{2\left(\lambda_c-\lambda\right)}{\lambda_c\left(\lambda_c-\lambda_o\right)}$	(B.14)

Table B.6: Expressions for the factors F_B and F_λ after application of the CZM formulation presented in [15, 17].

ACCEPTED MANUSCRIPT

Dependencies	Partial derivatives	
$\lambda_o(\mu_o)$	$\frac{\partial \lambda_o}{\partial \mu_o} = \frac{1}{K}$	(B.15)
$\lambda_c(\mu_o, \mathcal{G}_c)$	$\frac{\partial \lambda_c}{\partial \mu_o} = -\frac{2\mathcal{G}_c}{\mu_o^2}$	(B.16)
	$\frac{\partial \lambda_c}{\partial \mathcal{G}_c} = \frac{2}{\mu_o}$	(B.17)
$\mu_o(B)$	$\frac{\partial \mu_o}{\partial B} = \frac{\eta\left(\tau_{IIo}^2 - \tau_{Io}^2\right) B^{\eta-1}}{2\mu_o}$	(B.18)
$\mathcal{G}_c(B)$	$\frac{\partial \mathcal{G}_c}{\partial B} = \eta\left(\mathcal{G}_{IIc} - \mathcal{G}_{Ic}\right) B^{\eta-1}$	(B.19)
$\omega_d(\lambda_o, \lambda_c, \lambda)$	$\frac{\partial \omega_d}{\partial \lambda_o} = \frac{1}{2} K \lambda_c \frac{\lambda_o^2 - 2\lambda_c\lambda_o + \lambda_c\lambda}{(\lambda_o - \lambda_c)^2}$	(B.20)
	$\frac{\partial \omega_d}{\partial \lambda_c} = \frac{1}{2} K \lambda_o^2 \frac{\lambda_o - \lambda}{(\lambda_o - \lambda_c)^2}$	(B.21)
	$\frac{\partial \omega_d}{\partial \lambda} = \frac{1}{2} K \lambda_o \lambda_c \frac{1}{(\lambda_c - \lambda_o)}$	(B.22)
$\mathcal{D}^e(\omega_d, \mathcal{G}_c)$	$\frac{\partial\left(\frac{\omega_d}{\mathcal{G}_c}\right)}{\partial \omega_d} = \frac{1}{\mathcal{G}_c}$	(B.23)
	$\frac{\partial\left(\frac{\omega_d}{\mathcal{G}_c}\right)}{\partial \mathcal{G}_c} = \frac{-\omega_d}{\mathcal{G}_c^2}$	(B.24)
$\omega_{tot}(\lambda_o, \lambda_c, \lambda)$	$\frac{\partial \omega_{tot}}{\partial \lambda_o} = \frac{1}{2} K \lambda_c (\lambda_o - \lambda) \frac{\lambda - 2\lambda_c + \lambda_o}{(\lambda_o - \lambda_c)^2}$	(B.25)
	$\frac{\partial \omega_{tot}}{\partial \lambda_c} = \frac{1}{2} K \lambda_o \frac{(\lambda_o - \lambda)^2}{(\lambda_o - \lambda_c)^2}$	(B.26)
	$\frac{\partial \omega_{tot}}{\partial \lambda} = K \lambda_o \frac{\lambda_c - \lambda}{\lambda_c - \lambda_o}$	(B.27)
$\frac{\omega_{tot}}{\mathcal{G}_c}(\omega_{tot}, \mathcal{G}_c)$	$\frac{\partial\left(\frac{\omega_{tot}}{\mathcal{G}_c}\right)}{\partial \omega_{tot}} = \frac{1}{\mathcal{G}_c}$	(B.28)
	$\frac{\partial\left(\frac{\omega_{tot}}{\mathcal{G}_c}\right)}{\partial \mathcal{G}_c} = \frac{-\omega_{tot}}{\mathcal{G}_c^2}$	(B.29)

Table B.7: Dependencies and partial derivatives of the variables in the system using the CZM presented in [15, 17].

Highlights:

- The concept of growth driving direction for cohesive zone models is introduced.
- The growth driving direction is normal to the damage isolines.
- A point-wise criterion to predict the growth driving direction is formulated.
- Three different alternatives of the criterion are presented and discussed.
- The developed criteria can be applied to general 3D structures.